

Accretion Disk Size Measurements of Active Galactic Nuclei Monitored by the Zwicky Transient Facility

WEI-JIAN GUO,^{1,2} YAN-RONG LI ¹, ZHI-XIANG ZHANG,³ LUIS C. HO ⁴, AND JIAN-MIN WANG ^{1,2,5}

¹Key Laboratory for Particle Astrophysics, Institute of High Energy Physics, Chinese Academy of Sciences, 19B Yuquan Road, Beijing 100049, China;
Email: liyanrong@mail.ihep.ac.cn, wangjm@mail.ihep.ac.cn

²School of Astronomy and Space Science, University of Chinese Academy of Sciences, 19A Yuquan Road, Beijing 100049, China

³Department of Astronomy, Xiamen University, Xiamen, Fujian 361005, China

⁴Department of Astronomy, School of Physics, Peking University, Beijing 100871, China

⁵National Astronomical Observatories of China, Chinese Academy of Sciences, 20A Datun Road, Beijing 100020, China

Abstract

We compile a sample of 92 active galactic nuclei (AGNs) at $z < 0.75$ with *gri* photometric light curves from the archival data of the Zwicky Transient Facility and measure the accretion disk sizes via continuum reverberation mapping. We employ Monte Carlo simulation tests to assess the influences of data sampling and broad emission lines and select out the sample with adequately high sampling cadences (3 days apart in average) and minimum contaminations of broad emission lines. The inter-band time delays of individual AGNs are calculated using the interpolated cross-correlation function and then these delays are fitted with a generalized accretion disk model, in which inter-band time delays are a power function of wavelength, black hole mass, and luminosity. A Markov-chain Monte Carlo method is adopted to determine the best parameter values. Overall the inter-band time delays can be fitted with the $\tau \propto \lambda^{4/3}$ relation as predicted from a steady-state, optically thick, geometrically thin accretion disk, however, the yielded disk size is systematically larger than expected, although the ratio of the measured to theoretical disk sizes depend on using the emissivity- or responsivity-weighted disk radius. These results are broadly consistent with previous studies, all together raising a puzzle about the “standard” accretion disk model.

Keywords: Active galaxies (17); Supermassive black holes (1663); Reverberation mapping (2019); Galaxy accretion disks (562)

1. INTRODUCTION

Active galactic nuclei (AGNs) and quasars are those celestial objects that are believed to be powered by mass accretion onto the supermassive black hole (SMBH) residing in each (if not all) galactic center. The formed accretion disks surrounding SMBHs are responsible for the outward angular momentum transportation and huge energy radiation. In sub-Eddington regime, accretion disks are optically thick and geometrically thin and are described by the standard accretion disk model established by the pioneering work of Shakura & Sunyaev (1973). In super-Eddington regime, accretion disks become both optically and geometrically thick and are described by the slim disk model (Abramowicz et al. 1988; Wang et al. 1999). These accretion disk models had made great success in interpreting AGN observational characteristics (see Lin & Papaloizou 1996 for a review), such as the UV/optical continuum emissions (e.g., Koratkar & Blaes 1999; Kishimoto et al. 2008) and the broad spectral energy distributions (e.g., Sanders et al. 1989). Nevertheless, these models are still not fully understood and a variety of observational tests are clearly warranted (e.g., Courvoisier & Clavel 1991; Gierliński & Done 2004; Blaes 2007).

In practice, there are two direct methods to test for accretion disk models in AGNs. One method is through gravi-

tational microlensing (e.g., Kochanek 2004; Morgan et al. 2006) and the other is through continuum reverberation mapping (e.g., Collier et al. 1999; Cackett et al. 2007). In microlensing observations, disk sizes and radial temperature profiles are inferred by analyzing flux variability of multiple lensed images of gravitationally lensed quasars; In continuum reverberation mapping observations, measurements are a bit more straightforward. Inter-band time delays of AGN continuum light curves are interpreted to be the light-traveling time between different emission regions responsible for different wavelength bands. Therefore, such time delays directly provide constraints on physical disk sizes if multiplying the delays with the light speed (Collier et al. 1999). The dependence of time delays on wavelength can further determine radial temperature profiles of accretion disks. The both approaches generally found that the measured disk sizes are larger by a factor of about two than the anticipated values from the standard disk model (e.g., Morgan et al. 2010; Edelson et al. 2019; Cornachione & Morgan 2020 and references therein). This conflict had spurred great attention and a large number of studies to measure disk sizes and temperature profiles over the past decades.

Regarding continuum reverberation mapping, there are two major approaches: one approach utilizes space- and/or ground-based telescopes to monitor individual AGNs with

intensive cadences and multi-band filters (e.g., Fausnaugh et al. 2016, 2018; Starkey et al. 2016; McHardy et al. 2018; Cackett et al. 2018; Edelson et al. 2019; Cackett et al. 2020; Kara et al. 2021). This approach yields high-quality time delays and investigates in details disk structures in individual AGNs, but is apparently limited by telescope resources and sample size. The other approach largely relies on multi-band archival data of time-domain surveys and therefore can explore over large samples (e.g., Jiang et al. 2017; Mudd et al. 2018; Homayouni et al. 2019; Yu et al. 2020; Lobban et al. 2020; Homayouni et al. 2021; Jha et al. 2021). Despite the relatively poor quality in time delay measurements, the advantage of large sample sizes still makes this approach essential to draw meaningful constraints on disk structures. In particular, it allows to study the dependence of time delays on AGN properties (such as the luminosity, black hole mass, and accretion rate), therefore providing additional tests for accretion disk models.

In this work, we compile a sample of 92 AGNs from the Zwicky Transient Facility (ZTF) archives (Graham et al. 2019) with sufficient data quality of g -, r - and i -band photometric light curves to determine the inter-band time delays. We then use those time delays to investigate their dependence on various physical disk parameters, including black hole mass, mass accretion rate, and radial temperature profiles, aiming at measuring accretion disk structures. Compared to previous time-domain survey data, the ZTF data have a relatively more homogeneous and higher cadence (about 3 days apart) and lower measurement noises (typically $\lesssim 3\%$). These properties enable us to place more tight constraints on disk models.

The paper is organized as follows. Section 2 describes the data and sample selection based on the 3rd ZTF public data release. Section 3 generalizes the standard accretion disk model, in which inter-band time delays are formulated as a power function of wavelength, black hole mass, and luminosity. In Section 4, we use the obtained time delays to measure disk structures. Discussions and conclusions are given in Sections 5 and 6, respectively. Throughout the paper, we use a Λ CDM cosmology with $H_0 = 67 \text{ km s}^{-1} \text{ Mpc}^{-1}$, $\Omega_\Lambda = 0.68$, and $\Omega_m = 0.32$ (Planck Collaboration et al. 2020).

2. THE DATA AND SAMPLE

2.1. Photometric Light Curves and Spectra

The ZTF is a fully-automated time-domain survey aimed at a systematic exploration of the optical transient sky. It uses a 48-inch Schmidt telescope located at the Palomar Observatory, which is equipped with a wide-field camera (47 square degrees field of view) to photometrically scan the entire northern visible sky at a rate of ~ 3760 square degrees per hour (Bellm et al. 2019). There are three custom filters (g -, r -, and i -band) that cover a wavelength range approximately from 4100 \AA to 8700 \AA (Masci et al. 2019). The typical sampling interval is about three days (Graham et al. 2019).

We used the third ZTF public data release (DR3¹). When querying the data archives, we switched on the flag `catflags = 0` to filter out “bad-quality” data points (Masci et al. 2019). There are usually multiple exposures per night. We combined those exposures in average on the same night. The temporal baseline of DR3 spans two years (MJD 58200–58900) with a seasonal gap of about three months. The data in the first year have a relatively higher sampling rate, therefore, we only use the first-year data (MJD 58200–58400) for subsequent analysis. For the sake of illustration, Figure 1 plots the g -, r -, i -band light curves of a selected AGN.

To determine the black hole mass, optical luminosity at 5100 \AA , and broad emission line properties, we cross-matched the preselected sample with the quasar catalog of the 14th data release of the Sloan Digital Sky Survey² (DR14Q; Pâris et al. 2018). The redshift is limited to $z < 0.75$ to ensure the presence of broad $H\beta$ lines in spectra, with which the virial black hole mass can be estimated. There are about ten thousand AGNs at a redshift $z < 0.75$ with three-band data. Below we further censor those AGNs to select out ones with data quality sufficient to measure reliable inter-band delays.

2.2. AGN Properties

We employ a spectral decomposition scheme following Barth et al. (2013) and Hu et al. (2015) to derive the luminosity at 5100 \AA and emission line properties. We adopt the `DASpec` software³, which uses the Levenberg-Marquardt method for the chi-square optimization. The spectral components include a featureless power-law for the continuum, an Fe II template from Boroson & Green (1992), double Gaussians for the prominent broad emission lines (such as $H\alpha$, $H\beta$, $H\gamma$, He II, etc), a single Gaussian for the narrow emission lines (such as [O III] $\lambda\lambda 4959, 5007$, [O III] $\lambda 4363$, etc), a Balmer continuum, and a host galaxy template. For simplicity, the host galaxy template is chosen to be a single stellar population model with an instantaneous burst of 11 Gyr and a metallicity of $Z = 0.05$ from Bruzual & Charlot (2003). We derive the 5100 \AA luminosity from the power-law component, which means that the host galaxy component is naturally excluded. With the above spectral decomposition, we can also estimate the flux contributions of emission lines in each filter’s bandpass. Figure 2 shows an example of our spectral decomposition and the transmissions of the three ZTF filters.

Given with the 5100 \AA luminosity, the black hole mass is estimated by combining the size-luminosity ($R_{H\beta}$ - L_{5100}) scaling relation and $H\beta$ line widths ($V_{H\beta}$) from the single-epoch spectra, namely,

$$M_\bullet = f_{\text{BLR}} \frac{V_{H\beta}^2 R_{H\beta}}{G}, \quad (1)$$

¹ <https://www.ztf.caltech.edu>.

² <https://www.sdss.org/>

³ <https://github.com/PuDu-Astro/DASpec>

Table 1. Sample Properties

Object Name	R.A. (deg)	Dec. (deg)	z	$\log(M_{\bullet}/M_{\odot})$	$\log(L_{5100}/\text{erg s}^{-1})$	$\dot{\mathcal{M}}$	r_{gr}	r_{gi}	τ_{gr} (day)	τ_{gi} (day)
(1)	(2)	(3)	(4)	(5)	(6)	(7)	(8)	(9)	(10)	(11)
SDSS J002029.37+192153.0	5.1224	19.3647	0.627	8.56 ± 0.17	45.12 ± 0.05	1.09	0.82	0.83	$2.54^{+4.42}_{-4.41}$	$2.55^{+7.95}_{-5.93}$
SDSS J135955.65+504539.5	209.9819	50.7610	0.365	7.08 ± 0.17	44.67 ± 0.03	214.59	0.90	0.79	$-0.58^{+3.50}_{-3.30}$	$4.06^{+6.30}_{-8.91}$
SDSS J140201.84+443558.1	210.5077	44.5995	0.406	7.80 ± 0.15	44.70 ± 0.04	8.66	0.83	0.65	$-1.38^{+4.13}_{-4.28}$	$6.56^{+7.94}_{-11.91}$
SDSS J140604.24+572956.6	211.5177	57.4990	0.326	8.54 ± 0.14	44.25 ± 0.05	0.06	0.87	0.80	$-1.68^{+2.56}_{-2.82}$	$-2.03^{+8.88}_{-6.15}$
SDSS J141740.44+381821.1	214.4185	38.3059	0.450	7.76 ± 0.15	44.50 ± 0.04	5.40	0.89	0.68	$-4.10^{+4.37}_{-3.08}$	$-2.30^{+10.46}_{-11.24}$
SDSS J141956.64+583501.3	214.9860	58.5838	0.271	7.92 ± 0.16	44.32 ± 0.04	1.35	0.85	0.69	$4.85^{+2.44}_{-2.57}$	$6.86^{+4.89}_{-6.03}$

NOTE—Columns: (1) name, (2) right ascension, (3) declination, (4) redshift, (5) black hole mass, (6) optical luminosity at 5100 Å, (7) dimensionless accretion rate, (8) maximum cross-correlation coefficient between g - and r -band, (9) maximum cross-correlation coefficient between g - and i -band, (10) time delay between g - and r -band in the observed-frame, and (11) time delay between g - and i -band in the observed-frame. (This table is available in its entirety in machine-readable form.)

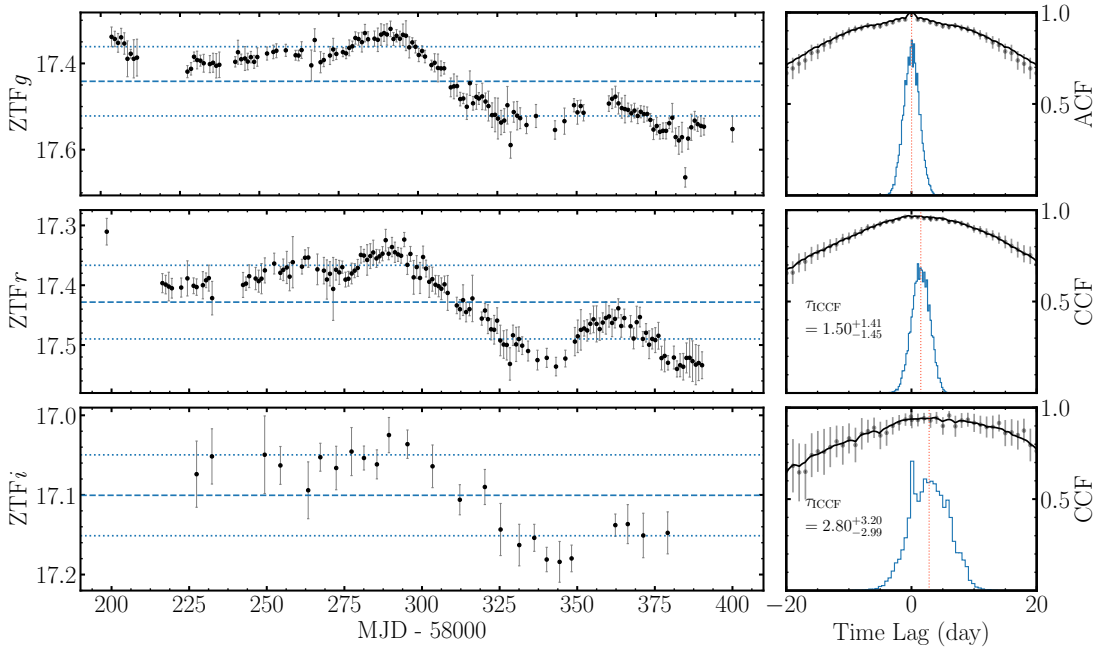


Figure 1. (Left) g -, r - and i -band light curves of an AGN selected from the ZTF DR3. Horizontal dashed and dotted lines represent the mean and 1σ fluxes of the light curves, respectively. (Right) from top to bottom panels are the ACF of the g -band light curve and the ICCFs of r - and i -band light curves with respect to g -band one, respectively. In each panel, the histogram represents the cross-correlation centroid distribution. Grey points with error bars show the ZDCFs.

where G is the gravitational constant, f_{BLR} is the virial factor, and $R_{\text{H}\beta}$ is determined from the $R_{\text{H}\beta}$ - L_{5100} relation. We use the $R_{\text{H}\beta}$ - L_{5100} relation compiled by Du & Wang (2019), which, compared to that compiled by Bentz et al. (2009, 2013), covers both sub- and super-Eddington AGNs and also takes into account the accretion rate,

$$\log(R_{\text{H}\beta}/\text{ld}) = \alpha_0 + \beta_0 \log \ell_{44} + \gamma_0 \mathcal{R}_{\text{Fe}}, \quad (2)$$

where $\ell_{44} = L_{5100}/10^{44} \text{erg s}^{-1}$ and \mathcal{R}_{Fe} is the flux ratio between Fe II and H β lines, which is strongly correlated with the accretion rate (e.g., Du et al. 2016). Here, the coefficient

values are $\alpha_0 = 1.65 \pm 0.06$, $\beta_0 = 0.45 \pm 0.03$, $\gamma_0 = -0.35 \pm 0.08$ (see Du & Wang 2019 for a detail). We use the full width at half maximum (FWHM) as the measure of H β line width and adopt a virial factor $f_{\text{BLR}} = 1.12 \pm 0.31$ (Woo et al. 2015).

In the following analysis, we also define the dimensionless accretion rate as (Du et al. 2014)

$$\dot{\mathcal{M}} = 20.1 \left(\frac{\ell_{44}}{\cos i} \right)^{3/2} m_7^{-2}, \quad (3)$$

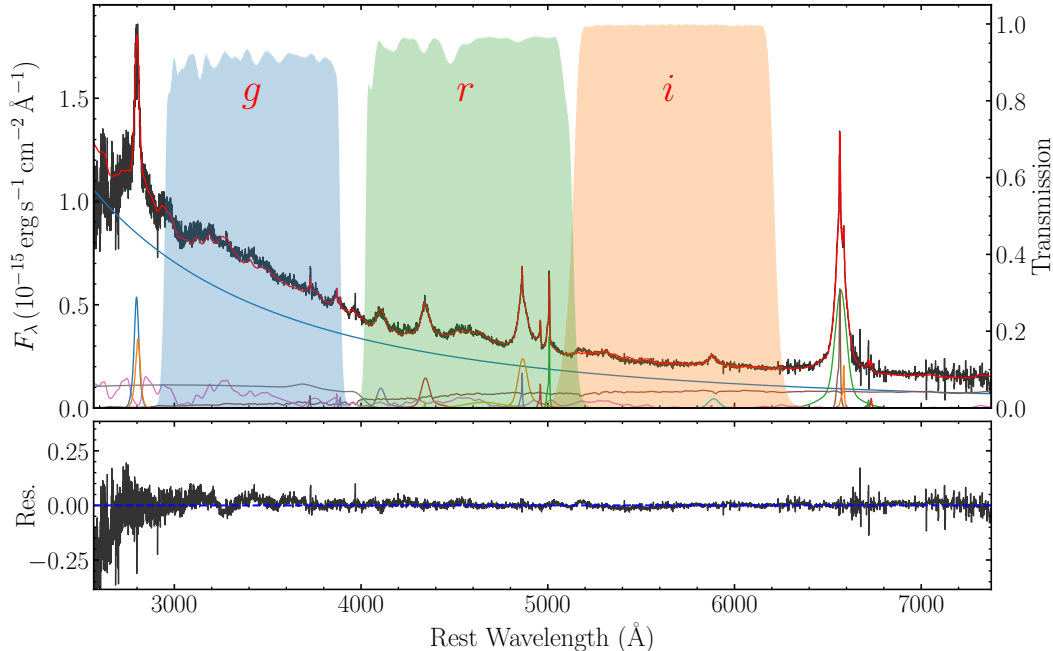


Figure 2. An example for our spectral decomposition. The top panel shows the fitting results and the bottom panel shows the residuals. Blue, green, yellow shaded areas represent the transmissions of g -, r -, and i -band filters, respectively.

where $m_7 = M_\bullet/10^7 M_\odot$ and i is the inclination angle of the accretion disk. We assume an averaged $\cos i \approx 0.75$, which corresponds to a typical inclination of AGNs with broad emission lines (e.g., Fischer et al. 2014; Du et al. 2016).

2.3. Time Delay Measurements

We first use the interpolated cross-correlation method to measure inter-band time delays between r/i -band and g -band light curves (Gaskell & Sparke 1986; Gaskell & Peterson 1987; Peterson 1993). The time delay is assigned the centroid of the interpolated cross-correlation functions (ICCFs) above 80% of the peak value. The associated uncertainties are estimated by 15.87% and 84.13% quantiles of the cross-correlation centroid distribution (CCCD), which is generated by the “Flux Randomization/Random Subset Selection (FR/RSS)” method (Peterson et al. 1998, 2004). The left panels of Figure 1 show the autocorrelation function (ACF), ICCF, and CCCD of the light curves for a selected AGN. The maximum cross-correlation coefficient r_{\max} and the measured time delays τ_{gr} and τ_{gi} are also listed in Table 1. For the sake of illustration, we also superimpose the z -transformed discrete correlation functions (ZDCFs; Alexander 1997, 2013) in Figure 1. The ZDCF method does not require interpolation to the light curves but is sensitive to binning in the correlation space and does not perform well for low-cadence data. We therefore do not use the ZDCF method for subsequent analysis.

In Appendix C, we use a model-independent approach, von Neumann estimator, to cross-check the ICCF results. The Von Neuman estimator is based on the regularity of randomness of data points in light curves (see Chelouche et al. 2017 for detail) and does not require an interpolation or binning

manipulation. In addition, we also employ the Bayesian analysis package MICA⁴ (Li et al. 2016). MICA uses the damped random walk model to describe the AGN variability (Kelly et al. 2009; Zu et al. 2013; Kasliwal et al. 2015) and a family of displaced Gaussians to approximate the transfer function between the driving and echoed light curves. MICA obtains the posterior distributions of the model parameters using the Markov-chain Monte Carlo technique with a diffusive nested sampling algorithm (Brewer et al. 2011; implemented by the package CDNest⁵). For simplicity, we only use one Gaussian in MICA and assign the time delay as the Gaussian center. As shown in Appendix C, we find general consistency among the ICCF, von Neumann estimator, and MICA methods.

2.4. Influences of Broad Emission Lines and Light Curve Sampling

There are two factors that may influence the obtained inter-band time delays. First, the presence of broad emission lines will cause shorter or longer time delays than the realistic values, depending on the flux contributions of the broad emission lines in each filter band-pass (see Section 5.1 below). Second, since the sampling intervals (~ 3 days) are comparable with or even longer than the anticipated time delays of accretion disks, the sampling rates and gaps in the light curves might be important and also affect the observed time delays. Below we employ Monte Carlo simulations to test

⁴ MICA is available at <https://github.com/LiyrAstroph/MICA2>.

⁵ CDNest is available at <https://github.com/LiyrAstroph/CDNest>.

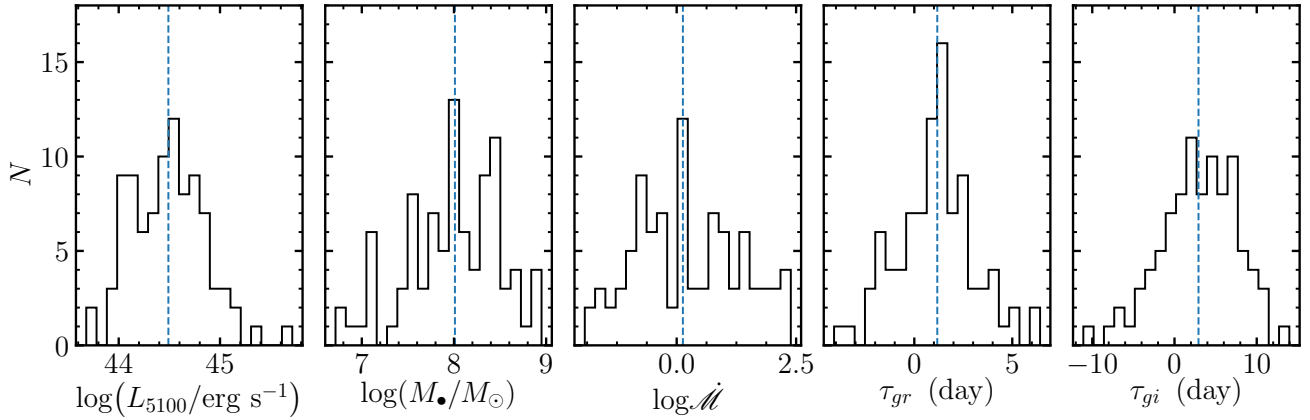


Figure 3. The histograms for luminosity at 5100Å, black hole mass, dimensionless accretion rate, inter-band time delays τ_{gr} and τ_{gi} (in the observed frame) from left to right panels. The blue lines represent the median values.

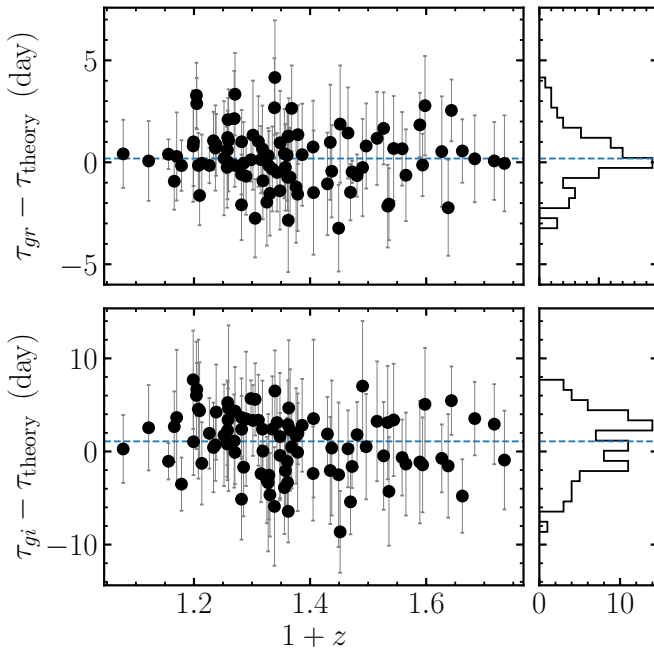


Figure 4. The differences of the rest-frame time delays of (top) r -band and (bottom) i -band with respect to g -band light curves compared to the corresponding theoretical delays based on the standard accretion disk model with $\chi = 5.04$.

these influences and select AGNs with minimized contaminations.

In simulations, we treat the g -band light curve as a realistic continuum light curve without contaminations of broad emission lines for the sake of simplicity. We first employ the damped random walk model (Kelly et al. 2009; Zu et al. 2013) to reconstruct the continuum light curves. Using the black hole mass and luminosity obtained from the spectral decomposition, we calculate the theoretical time delays of r - and i -bands with respect to g -band based on the standard accretion disk model (see Section 3.1 below). We generate mock r/i -band continuum light curves by shifting the recon-

structed g -band light curve with the theoretical time delays and then interpolate them onto the observed time epochs. To generate mock light curves of broad emission lines, we assume that all emission lines have the same time delays as derived from the $R_{H\beta}-L_{5100}$ scaling relation and the corresponding transfer function is Gaussian with a width set to a quarter of the time delay. We convolve the reconstructed g -band continuum light curve with this Gaussian transfer function and scale the obtained light curve to force the same flux contribution in $g/r/i$ band as in the spectral decomposition. We finally add up light curves of the continuum and emission lines to create the contaminated mock g -, r -, and i -band light curves and assign the uncertainties by the relative errors of the observed light curves. We calculate the time delays of mock light curves using the same interpolated cross-correlation method as applied to the observed light curves. In Appendix A, we show examples of mock light curves and the corresponding ICCF results.

By repeating the above procedure 5000 times, we obtain time delay distributions of r and i bands for each AGN in the sample. We calculate means from the distributions and assign their uncertainties by the 68.3% confidence intervals. We first discard those AGNs with mock uncertainties larger than 12 days, which indicates poor data quality. From the remaining AGNs, if the mean delay is consistent with the input value within the mock uncertainties, we mark that the corresponding observed time delay is reliable and the influences of emission lines and/or data sampling are minimized.

2.5. Sample Selection Criteria

We design the following criteria to select those AGNs that have sufficiently good data quality to reliably measure inter-band time delays.

- Both g - and r -band light curves have epochs $N_{g,r} \geq 60$ over the time baseline of ~ 200 days. Because the r -band sampling rate is relatively low, we relax the criteria to epochs $N_i \geq 20$.

- The g -, r - and i -band light curves have statistically significant variability with $\sigma^2 \geq \Delta^2$, where

$$\sigma^2 = \sum_{j=1}^n \frac{(F_j - \langle F \rangle)^2}{N-1}, \quad \Delta^2 = \sum_{j=1}^n \frac{\Delta_j^2}{N}. \quad (4)$$

where N is the epoch number, F_j and Δ_j are the flux and measurement error at the j -th epoch, respectively, and $\langle F \rangle$ is the averaged flux.

- The ICCFs of the r - and i -band light curves are calculated with respect to the g -band light curve. The maximum cross-correlation coefficients are restricted to $r_{\max} > 0.8$ for r -band and $r_{\max} > 0.6$ for i -band.
- The ACF FWHM of the g -band light curve is restricted to < 80 days. This is devised to discard those light curves with little variation patterns so that the cross-correlation analysis usually has difficulty in determining the time delay.
- As described in 2.4, the uncertainties of time delays for mock light curves are restricted to < 12 days and the differences between the mock time delay and the input values are within the uncertainties.

We finally obtain a sample of 92 AGNs. In Table 1, we summarize the basic properties of the sample. In Figure 3, we plot the distributions of 5100 Å luminosity (L_{5100}), black hole mass (M_{\bullet}), dimensionless accretion rate ($\dot{\mathcal{M}}$), and inter-band time delays (τ_{gr} and τ_{gi}) of the sample. Overall, the black hole mass ranges from 10^7 to $10^9 M_{\odot}$, the dimensionless accretion rate ranges from ~ 0.01 to 100, and the 5100 Å luminosity ranges from 10^{44} to 10^{45} erg s $^{-1}$. The inter-band time delays are on the order of days and τ_{gr} is generally smaller than τ_{gi} as expected. In Figure 4, we show the residuals between the observed inter-band time delays and theoretical delays based on the standard accretion disk model with $\chi = 5.04$ (see Section 3 below).

3. ACCRETION DISK MODELS

3.1. The Standard Accretion Disk Model

In the standard accretion disk model, by assuming a Keplerian rotation, the effective temperature T at radius R can be obtained by equating the radiated flux per disk's surface area to the viscous dissipation rate

$$\sigma T^4 = \frac{3GM_{\bullet}\dot{M}}{8\pi R^3}, \quad (5)$$

where σ is the Stefan-Boltzmann constant and \dot{M} is the mass accretion rate. To establish the relation between the wavelength and time delay, we perform the following manipulations. At a given wavelength λ , the temperature is

$$T = \frac{hc}{k\lambda}, \quad (6)$$

which corresponds to a radius using Equation (5)

$$\begin{aligned} R_{\lambda} &= \left(\frac{3Gk^4}{8\pi\sigma h^4 c^4} \right)^{1/3} M_{\bullet}^{1/3} \dot{M}^{1/3} \lambda^{4/3} \\ &= \left(\frac{3GC_{\text{bol}}k^4}{8\pi\sigma\eta h^4 c^6} \right)^{1/3} M_{\bullet}^{1/3} L_{5100}^{1/3} \lambda^{4/3}, \end{aligned} \quad (7)$$

where h is the Planck constant, k is the Stefan-Boltzmann constant, $C_{\text{bol}} = 9.26$ is the bolometric correction factor for the 5100 Å luminosity L_{5100} (Shen et al. 2008; Sánchez-Sáez et al. 2018), $\eta = 0.1$ is the radiative efficiency, and \dot{M} is related to L_{5100} as

$$\dot{M} = \frac{C_{\text{bol}}L_{5100}}{\eta c^2}. \quad (8)$$

The observed time delay represents the weighted radius of regions that radiate photons at the wavelength λ , namely,

$$c\tau_{\lambda} = \langle R \rangle_{\lambda} = \chi R_{\lambda}. \quad (9)$$

where $\langle R \rangle_{\lambda}$ represents the weighted radius and χ is a multiplicative factor. Combining Equations (7) and (9) gives

$$c\tau_{\lambda} = \left(\frac{3GC_{\text{bol}}k^4 X^4}{8\pi\sigma\eta h^4 c^6} \right)^{1/3} M_{\bullet}^{1/3} L_{5100}^{1/3} \lambda^{4/3}, \quad (10)$$

where we use the conventional quantity in the literature

$$X \equiv X_{\text{ss}} = \chi^{3/4}. \quad (11)$$

Here, the subscript “ss” represents the standard accretion disk and X (or χ) is introduced to account for the fact that a broad range of disk radius emits photons of a given wavelength. Below we will show how to calculate the values of χ and X (see Equations 19 and 23).

In reality, we measure time delays with respect to a reference wavelength, say, e.g., λ_0 . According to Equation (10), the observed time delay is then written as

$$\tau(\lambda) = \tau_{\text{d}}(\lambda_0) \left[\left(\frac{\lambda}{\lambda_0} \right)^{4/3} - 1 \right], \quad (12)$$

where τ_{d} is the time delay at the wavelength λ_0 , depending on black hole mass and luminosity. For a large sample of AGNs with different redshifts, black hole masses, and luminosities, it is more convenient to set the reference wavelengths to a fixed common rest-frame wavelength (λ_0) and normalize the coefficient τ_{d} with respect to a fixed black hole mass and luminosity. As such, the observed time delay (in the observed frame) between two wavelength bands (say, λ_1 and λ_2 ; also in the observed frame) for an AGN at a redshift z is then given by

$$\tau_{\text{obs}} = \tau_{\text{d}} M_8^{1/3} \ell_{44.5}^{1/3} (1+z)^{-1/3} \left[\left(\frac{\lambda_1}{\lambda_0} \right)^{4/3} - \left(\frac{\lambda_2}{\lambda_0} \right)^{4/3} \right], \quad (13)$$

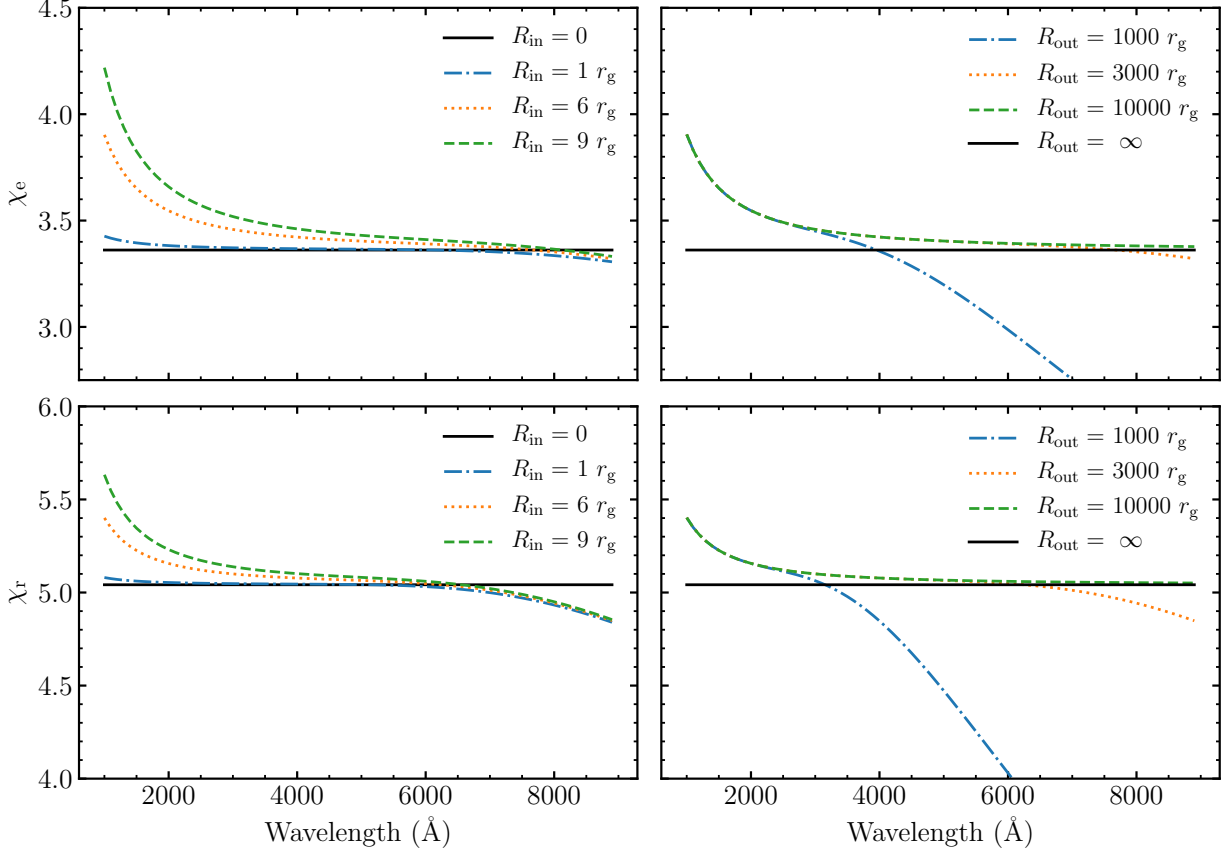


Figure 5. The emissivity-weighted factor χ_e (top) and responsivity-weighted factor χ_r (bottom) with wavelength for different inner and outer disk radius under the standard disk model. In left panels $R_{\text{out}} = 3000r_g$ and in right panels $R_{\text{in}} = 6r_g$. The black line in each panel corresponds to $R_{\text{in}} \rightarrow 0$ and $R_{\text{out}} \rightarrow \infty$.

where $M_8 = M_\bullet/10^8 M_\odot$, $\ell_{44.5} = L_{5100}/10^{44.5} \text{ erg s}^{-1}$, and τ_d denotes the time delay at the wavelength λ_0 (in the rest frame) with $M_\bullet = 10^8 M_\odot$ and $L_{5100} = 10^{44.5} \text{ erg s}^{-1}$. For the standard accretion disk, τ_d is given by

$$\begin{aligned} \tau_d &= \frac{1}{c} \left(\frac{3GC_{\text{bol}}k^4 X_{\text{ss}}^4}{8\pi\sigma\eta h^4 c^6} \right)^{1/3} \\ &\times (10^8 M_\odot)^{1/3} (10^{44.5} \text{ erg s}^{-1})^{1/3} \lambda_0^{4/3} \\ &= 0.67 X_{\text{ss}}^{4/3} (\lambda_0/7000\text{\AA})^{4/3} \text{ light-day}. \end{aligned} \quad (14)$$

3.2. Generalizing the Standard Accretion Disk Model

Equation (13) illustrates the time delay as a function of black hole mass, luminosity, and wavelength under the standard accretion disk model. We generalize Equation (13) into a form of (see also Homayouni et al. 2019)

$$\tau_{\text{obs}} = \tau_0 (1+z)^{1-\beta} M_8^\gamma \ell_{44.5}^\delta \left[\left(\frac{\lambda_1}{\lambda_0} \right)^\beta - \left(\frac{\lambda_2}{\lambda_0} \right)^\beta \right], \quad (15)$$

where τ_0 , β , γ , and δ are free parameters. The physical meanings of the above parameters can be understood as follows. Equation (15) corresponds to a relation between the temper-

ature and radius as

$$\sigma T^4 = \left(\frac{\tau_0}{\tau_x} \right)^{4/\beta} \frac{3GM_\bullet^{4\gamma/\beta} \dot{M}^{4\delta/\beta}}{8\pi R^{4/\beta}}, \quad (16)$$

where τ_x is given by

$$\begin{aligned} \tau_x &= \frac{1}{c} \left(\frac{3Gk^4 X^4}{8\pi\sigma h^4 c^4} \right)^{\beta/4} \left(\frac{C_{\text{bol}}}{\eta c^2} \right)^\delta \\ &\times (10^8 M_\odot)^\gamma (10^{44.5} \text{ erg s}^{-1})^\delta \lambda_0^\beta, \end{aligned} \quad (17)$$

and

$$X = \chi^{1/\beta}. \quad (18)$$

As can be seen, τ_0 measures the disk size, β controls the temperature profile with radius, and γ and δ control the dependence of the radiated flux per disk's surface area on black hole mass and accretion rate, respectively. By setting $\tau_0 = \tau_d$, $\beta = 4/3$, $\gamma = 1/3$, and $\delta = 1/3$, we return to the case of the standard accretion disk model and $\tau_x = \tau_d$. It is worth stressing that for a general set of β , γ , and δ , τ_x no longer has the dimension of time and therefore does not indicate the disk size. Below we use this generalized Equation (15) to fit the observation data.

Table 2. The multiplicative factors χ and X in the case of $R_{\text{in}} = 0$ and $R_{\text{out}} = \infty$.

β	Emissivity Weighting		Responsivity Weighting	
	χ	X	χ	X
1	1.46	1.46	2.19	2.19
4/3	3.36	2.49	5.04	3.37
5/3	7.81	3.43	11.71	4.37
2	18.80	4.36	28.19	5.38

3.3. The Multiplicative Factor χ

In the literature, there are two approaches for calculating the weighted radius $\langle R \rangle_\lambda$. One approach is emissivity weighting and the other is responsivity weighting (Starkey et al. 2016; Tie & Kochanek 2018). For emissivity weighting, the multiplicative factor is directly given by

$$\chi \equiv \chi_e = \frac{1}{R_\lambda} \frac{\int_{R_{\text{in}}}^{R_{\text{out}}} B_\lambda(T) R^2 dR}{\int_{R_{\text{in}}}^{R_{\text{out}}} B_\lambda(T) R dR}, \quad (19)$$

where the subscript “e” represents emissivity weighting, R_{in} and R_{out} are the inner and outer radius of the accretion disk, respectively, and $B_\lambda(T)$ is the Planck function of a temperature T at a wavelength λ ,

$$B_\lambda(T) = \frac{2hc}{\lambda^3} \frac{1}{e^{hc/\lambda kT} - 1}. \quad (20)$$

For the case of responsivity weighting, we follow the procedure of Starkey et al. (2017) and Tie & Kochanek (2018) to calculate the multiplicative factor. Specifically, the radiated thermal energy of each annuli of the accretion disk responds to the incident driving variations as

$$\sigma T^4(t) = \sigma T_0^4 [1 + f_c(t - R/c)], \quad (21)$$

where T_0 represents the unperturbed temperature of the accretion disk and f_c represents the fraction of incident energy flux thermalized by the disk annuli. For small variations, Equation (21) effectively leads to a temperature fluctuation as

$$\frac{\partial T(t)}{\partial f_c} \approx \frac{T}{4}. \quad (22)$$

As a result, the multiplicative factor χ is given by

$$\chi \equiv \chi_r = \frac{1}{R_\lambda} \frac{\int_{R_{\text{in}}}^{R_{\text{out}}} \frac{\partial B_\lambda(T)}{\partial T} \frac{\partial T}{\partial f_c} R^2 dR}{\int_{R_{\text{in}}}^{R_{\text{out}}} \frac{\partial B_\lambda(T)}{\partial T} \frac{\partial T}{\partial f_c} R dR}, \quad (23)$$

where the subscript “r” represents responsivity weighting.

In Appendix B, we show how to calculate the two multiplicative factors. The two factors depend on the inner and outer disk radius and generally change with wavelength. In

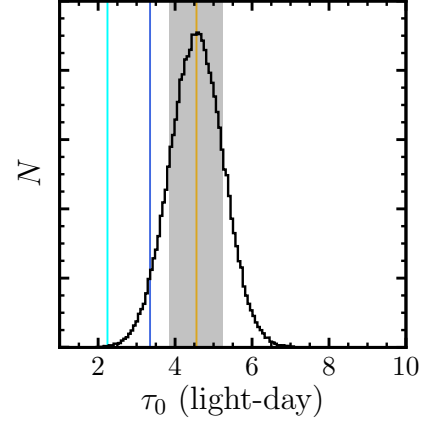


Figure 6. The posterior distribution of the disk size τ_0 under Case I. The shaded area represents the 68.3% confidence interval and the yellow vertical line represent the best estimate. The blue and cyan lines represent the anticipated disk sizes ($\tau_0 = 3.35$ and 2.24 light-days) of the standard accretion disk model with $\chi = 5.04$ and 3.36, respectively.

extreme cases of $R_{\text{in}} \rightarrow 0$ and $R_{\text{out}} \rightarrow \infty$, the two factors are independent on wavelength and can be expressed analytically with the help of the zeta and gamma functions. Table 2 lists values of the two factors with different temperature profiles with $R_{\text{in}} \rightarrow 0$ and $R_{\text{out}} \rightarrow \infty$. For the standard accretion disk model ($\beta = 4/3$), we have $\chi_e = 3.36$ and $\chi_r = 5.04$, which correspond to $X = 2.49$ and 3.36, respectively. Table 2 also illustrates that the two factors sensitively change with temperature profiles. As β increases from 1 to 2, both χ_e and χ_r increase by more than one order of magnitude.

For finite inner and outer disk radius, χ_e and χ_r can only be calculated numerically. In Figure 5, we plot the two factors with different inner and outer disk radius under the standard disk model ($\beta = 4/3$). Both χ_e and χ_r increase with the inner/outer disk radius because of the increasing fraction of radiation from large disk annulus. Moreover, as expected, the inner (outer) disk radius mainly affects the factors at short (long) wavelength.

It is worth stressing that the disk size measurement through fitting inter-band time delays does not rely on the multiplicative factor. It is only required when comparing the measured disk size against the disk model.

4. MEASURING ACCRETION DISK STRUCTURES

We use Equation (15) to fit the observed time delays from ICCF analysis. The present sample size does not allow us to reliably constrain the full parameters (τ_0 , β , γ , and δ). Therefore, inspired by the energy equation of the generalized accretion disk model (see Equation 16), we design the following cases by fixing some of the parameters.

- Case I: fixing $\beta = 4/3$, $\gamma = 1/3$, and $\delta = 1/3$.

In this case, only τ_0 is free to determine so that we can test the standard accretion disk model by comparing the obtained τ_0 against the anticipated value.

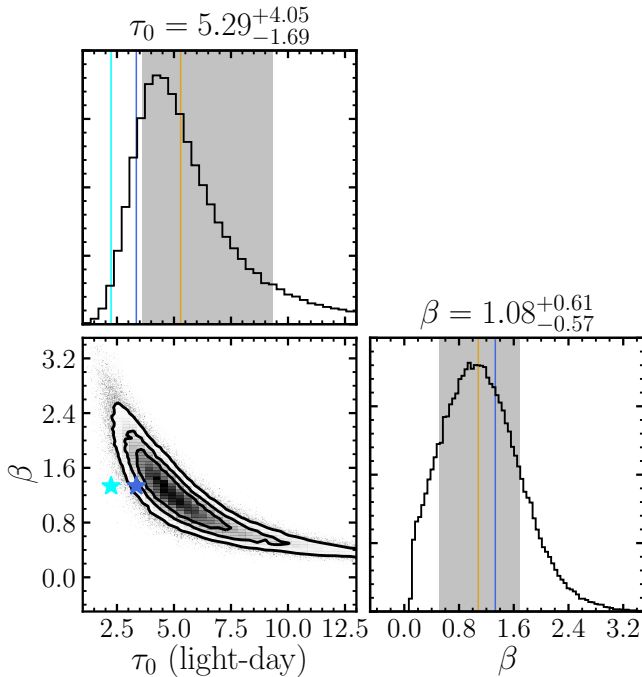


Figure 7. The posterior distributions of the disk size τ_0 and temperature profile parameter β for Case II. The orange lines and grey shaded bands show the median values and 68.3% confidence intervals. For τ_0 , the blue and cyan lines (stars) show the theoretical values of the standard accretion disk model with $\chi_e = 3.36$ and $\chi_r = 5.04$, respectively. For β , the blue line (stars) shows the theoretical value of $4/3$. The contours are at 1σ , 1.5σ , and 2σ levels.

- Case II: fixing $\gamma/\beta = 1/4$ and $\delta/\beta = 1/4$.
In this case, τ_0 and β are free parameters to determine so that we measure the disk size and temperature profile simultaneously.
- Case III: fixing $\beta = 4/3$.
In this case, the disk’s temperature profile is the same as in the standard accretion disk model. The rest parameters τ_0 , γ , and δ are free to determine.

Table 3 summarizes the fixed parameters in the above three cases. We employ a Markov-chain Monte Carlo method implemented with the `emcee`⁶ package to optimize the fitting (Foreman-Mackey et al. 2013). We assign the best values by the medians and the uncertainties by the 68.3% confidence intervals of posterior distributions of the parameters. We adopt a logarithm prior for τ_0 and uniform priors for the rest parameters. The prior range for τ_0 is (0, 10) light-days, for β is (0, 5), for γ is (−1, 1), and for δ is (−1, 1). In Table 3, we also list the inferred best values and uncertainties of the parameters. Below we present the results for each case.

4.1. Case I

In this case, we fix $\beta = 4/3$, $\gamma = 1/3$, and $\delta = 1/3$, and only set τ_0 free. Figure 6 shows the obtained posterior

distribution of τ_0 . The best estimate is $\tau_0 = 4.56^{+0.69}_{-0.69}$ light-days. This value is about 1.36 times the prediction of 3.35 light-days with $\chi_r = 5.04$ at a 2σ level and 2.06 times the prediction of 2.24 light-days with $\chi_e = 3.36$ at a 3σ level.

4.2. Case II

In this case, we fix $\gamma = \beta/4$ and $\delta = \beta/4$ but set τ_0 and β free. This means that the radiated flux per unit disk’s surface area linearly depends on black hole mass and accretion rate as in the standard accretion disk model (see Equation 16), namely,

$$\sigma T^4 \propto M_\bullet \dot{M}. \quad (24)$$

Figure 7 plots the posterior distributions of τ_0 and β . The disk size parameter τ_0 is strongly anti-correlated with the temperature profile parameter β as implied from Equation (15). Because of the limited redshift range and wavelength coverage of the present sample, there appears a long tail toward the corner of small β and large τ_0 in the contour between τ_0 and β . The best estimate for τ_0 is $5.29^{+4.05}_{-1.69}$ light-days, consistent within uncertainties with the inferred value of Case I. The best estimate of $\beta = 1.08^{+0.61}_{-0.57}$, in agreement with uncertainties with the fiducial value of $4/3$ for the standard accretion disk model.

4.3. Case III

In this case, we fix $\beta = 4/3$ to force the temperature profile to follow the same radial dependence ($T \propto R^{-3/4}$) as in the standard accretion disk model. Figure 8 shows the posterior distributions of τ_0 , γ , and β . The inferred disk size is $\tau_0 = 4.68^{+0.88}_{-0.91}$ light-days, again consistent within uncertainties with the measurements of Cases I and II. The parameter of $\delta = 0.44^{+0.19}_{-0.22}$ remarkably agrees with the fiducial value of $1/3$ for the standard disk model (see Equation 13). However, the parameter $\gamma = 0.06^{+0.15}_{-0.15}$, lower than the fiducial value of $1/3$ at a 2σ level. This discrepancy may arise from the adopted virial factor f_{BLR} that neglects the dependence on black hole mass.

4.4. Comparisons with Previous Studies

There were several previous studies that measured accretion disk sizes using AGN samples from time-domain surveys (see Table 4 for a brief summary). Homyouni et al. (2019) analyzed continuum time delays between *i* and *g* bands of 95 quasars in the Sloan Digital Sky Survey Reverberation Mapping project and did not find evidence that the derived disk size deviates from the theoretical expectation of the standard accretion disk model. Mudd et al. (2018) and Yu et al. (2020) measured disk sizes of 15 and 22 quasars using *griz* light curves selected from different fields of the Dark Energy Survey, respectively. They both drew a similar conclusion as Homyouni et al. (2019). However, Homyouni et al. (2021) used UV-optical continuum reverberation mapping observations of eight quasars and found that the disk size is 2–4 times the expectation of the standard accretion disk model if assuming $\chi = 3.36$. Jiang et al. (2017) performed disk size measurements of 39 AGNs based on the *griz* light

⁶ `emcee` is available at <https://github.com/dfm/emcee>.

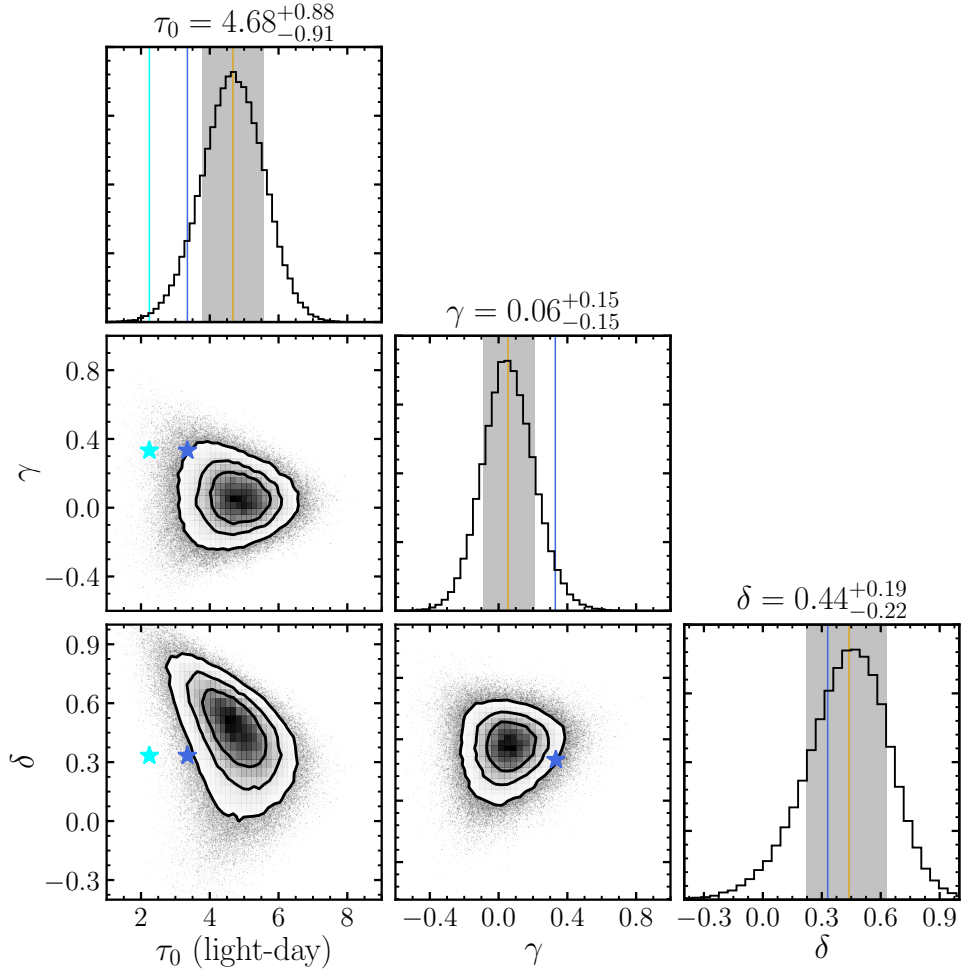


Figure 8. The posterior distributions of τ_0 , γ and δ for Case III. The orange lines and grey shaded bands show the median values and 68.3% confidence intervals. For τ_0 , the blue and cyan lines (stars) show the theoretic values from the standard accretion disk model with $\chi_e = 3.36$ and $\chi_r = 5.04$, respectively. For other parameters, the blue lines (stars) show the theoretical values. The contours are at 1σ , 1.5σ , and 2σ levels.

Table 3. Three cases of fitting and the inferred values of parameters.

	Case	τ_0 (light-day)	β	γ	δ
Prior	Case I	LogUniform(0, 10)	fixed(4/3)	fixed(1/3)	fixed(1/3)
	Case II	LogUniform(0, 10)	Uniform(0, 5)	fixed($\beta/4$)	fixed($\beta/4$)
	Case III	LogUniform(0, 10)	4/3	Uniform(-1, 1)	Uniform(-1, 1)
Posterior	Case I	$4.56^{+0.69}_{-0.69}$
	Case II	$5.29^{+4.05}_{-1.69}$	$1.08^{+0.61}_{-0.57}$
	Case III	$4.68^{+0.88}_{-0.91}$...	$0.06^{+0.15}_{-0.15}$	$0.44^{+0.19}_{-0.22}$

Table 4. A summary of disk size measurements.

Data	Sample Size	Median Cadence	Duration	Bands	RM	Reference
Pan-STARRS	39	3 days	3.3 years	g, r, i, z	No	Jiang et al. (2017)
OzDES	15	7 days	180 days	g, r, i, z	No	Mudd et al. (2018)
SDSS-RM	95	4 days	180 days	g, i	Yes	Homayouni et al. (2019)
OzDES	23	2 days	3.3 years	g, r, i, z	No	Yu et al. (2020)
ZTF	19	3 days	3 years	g, r, i	Yes	Jha et al. (2021)
ZTF	92	3 days	200 days	g, r, i	No	This Work

NOTE—“RM” means reverberation mapping of broad emission lines, from which black hole mass can be estimated, instead of using the $R_{H\beta}$ - L_{5100} relation.

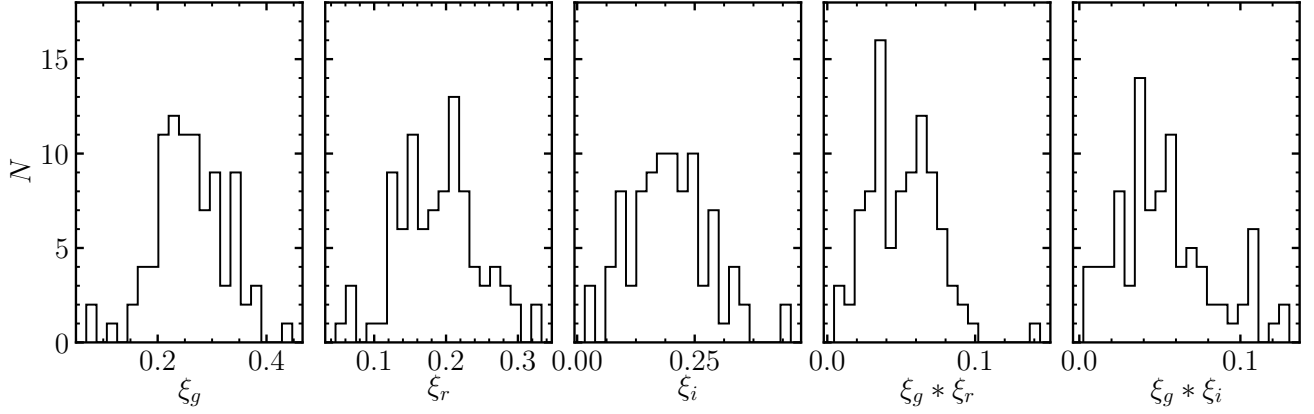


Figure 9. The three left panels are the flux fractions of broad emission lines in g , r and i bands respectively. The rightmost two panels are products of the flux fractions of broad emission lines in gr and gi bands.

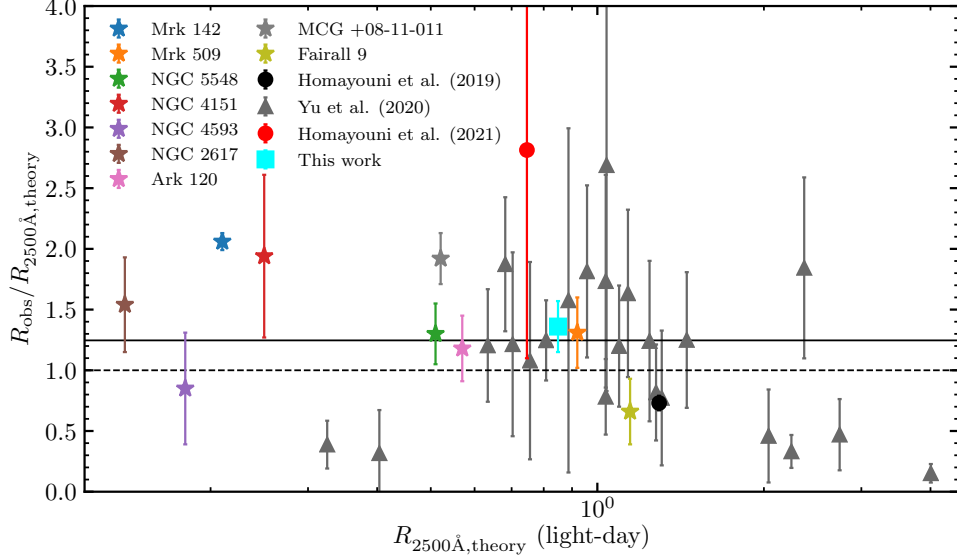


Figure 10. The ratio of the measured disk size to theoretical size at 2500 \AA based on the standard accretion disk model with the multiplicative factor $\chi = 5.04$. The solid line represent the median ratio 1.24 and the dashed line represent the ratio equal to one.

curves from the Pan-STARRS survey and also concluded that the disk sizes were bigger than expected by a factor of 2-3 with $\chi = 3.36$. Recently, [Jha et al. \(2021\)](#) cross matched the previously reverberation-mapped AGNs (using the broad H β line) with the ZTF archival data and compiled a sample of 19 AGNs. Their obtained disk sizes are also found to be larger than expected (with $\chi = 3.36$).

The high-precision measurements from individual nearby AGNs also generally indicated a disk size larger by a factor of 2-3 than the theoretical expectation (e.g., [Fausnaugh et al. 2016](#); [Cackett et al. 2018](#); [Edelson et al. 2019](#)). However, an exception is Fairall 9, which shows a delay spectrum following the standard accretion disk model ([Hernández Santisteban et al. 2020](#)) in both amplitude and power index. These studies generally adopted $\chi = 3.36$.

As a comparison, our results in all three cases show that regardless of emissivity weighting ($\chi = 3.36$) or responsivity weighting ($\chi = 5.04$), the disk size is larger than the theoretical expectation. In Figure 10, we plot the ratio of the inferred to the theoretical disk sizes from previous studies and this work. For the sake of consistency, we uniformly use the same factor of responsivity weighting, namely, $\chi = 5.04$. In addition, different studies reported disk sizes at different reference wavelengths. We uniformly convert the reference wavelength to 2500 Å using a relation $\tau_{0,2500\text{Å}}/\tau_{0,\lambda_0} = (\lambda_0/2500\text{Å})^{-4/3}$ based on the standard accretion disk model. Figure 10 implies that if regardless of the large scatters, the averaged disk size is still larger than the theoretical size. The median ratio of the measured to theoretical disk sizes is 1.24.

As for the temperature profile, our results agree with previous studies (e.g., [Homayouni et al. 2019](#); [Cackett et al. 2018](#); [Edelson et al. 2019](#)), which overall found $\tau \propto \lambda^{4/3}$ as expected from the standard accretion disk model, although our results have relatively large uncertainties due to the limited sample size and filters.

5. DISCUSSIONS

5.1. The Influences of Broad Emission Lines

In Section 2.4, we assess the influences of broad emission lines through Monte Carlo simulations and select out the final sample with the minimum influences. Here we make a more thorough discussion. In the presence of broad emission lines, the light curve in each band has an additional component, i.e., $f_X = f_X^c + f_X^l$, where the superscript ‘‘c’’ denotes the intrinsic continuum flux and ‘‘l’’ denotes the line flux. The cross-correlation function (CCF) between light curves of two bands, say, X and Y , is then given by

$$\begin{aligned} \text{CCF}(f_X, f_Y) &= \frac{E[(f_X - \bar{f}_X)(f_Y - \bar{f}_Y)]}{\sigma[f_X]\sigma[f_Y]} \\ &= (1 - \xi_X)(1 - \xi_Y)\text{CCF}(f_X^c, f_Y^c) \\ &\quad + \xi_X(1 - \xi_Y)\text{CCF}(f_X^l, f_Y^c) \\ &\quad + (1 - \xi_Y)\xi_X\text{CCF}(f_X^c, f_Y^l) \\ &\quad + \xi_X\xi_Y\text{CCF}(f_X^l, f_Y^l), \end{aligned} \quad (25)$$

where E and σ represent the expectation and standard deviation of the light curves, and $\xi_X = f_X^l/(f_X^c + f_X^l)$ and $\xi_Y = f_Y^l/(f_Y^c + f_Y^l)$ represent the flux fractions in X and Y bands contributed from broad emission lines, respectively. For simplicity, we assume a common characteristic time delay of τ_{BLR} for all broad emission lines. In the far right-hand side of Equation (25), the second and third terms give rise to CCF peaks at about $-\tau_{\text{BLR}}$ and $+\tau_{\text{BLR}}$, respectively. The fourth term yields a CCF peak at zero time delay. It is clear that the influences of these terms to the final time delay depend on ξ_X , ξ_Y and their product $\xi_X * \xi_Y$.

- If $\xi_X > \xi_Y$, the second term will be dominated over the other two terms and therefore the resulting time delay will tend to be shortened (compared with that without broad emission lines).
- If $\xi_X < \xi_Y$, we have the opposite case and the time delay will tend to be enlarged.
- If $\xi_X \rightarrow 1$ and $\xi_Y \rightarrow 1$, the fourth term will be dominated and the time delay tends to be zero.

In Figure 9, we show the flux fractions of broad emission lines in g , r , and i bands, together with their products. We find that generally $\xi_g > \xi_r$ and $\xi_g > \xi_i$, implying that the presence of broad emission lines tends to shorten the time delays. In Appendix A, we perform simulations to illustrate how time delays are quantitatively affected for different flux fractions of broad emission lines, which is in agreement with the above simple arguments.

5.2. The Selection Criteria

To test the influences of the selection criteria in Section 2.5, we adjust the restrictions on the ACF FWHM and mock uncertainties and repeat the above analysis procedures for Case I. In the left panel of Figure 11, we restrict the ACF FWHM to be smaller than 90, 80, and 70 days and obtain the disk size $\tau_0 = 4.51^{+0.68}_{-0.67}$, $4.56^{+0.69}_{-0.69}$, and $4.59^{+0.72}_{-0.72}$ days, respectively. As the restriction of the ACF FWHM decreases, the inferred disk size is almost unchanged, indicating that it is insensitive to the limit of the ACF FWHM. Meanwhile, the AGN sample size is reduced from 96 to 87, but the quality of the inter-band time delays improve in terms of errors. These two factors lead to almost similar uncertainties of the inferred disk sizes for different criteria of the ACF FWHM. This also plausibly implies that the bigger-than-expected disk size is true and not caused by measurement errors.

In the right panel of Figure 11, we set an upper limit of the mock uncertainty of the simulated light curves $\sigma_\tau < 10$, 12, and 14 days (see Section 2.4). The correspondingly disk sizes are $\tau_0 = 4.62^{+0.74}_{-0.75}$, $4.56^{+0.69}_{-0.69}$, and $4.35^{+0.65}_{-0.65}$ days, respectively. The inferred disk size gets slightly larger as σ_τ decreases (but is consistent within uncertainties). Meanwhile, the associated uncertainty slightly increases because the AGN number decreases (from 110 to 75). A lower limit of σ_τ means that AGNs with relatively higher-quality time delays will be selected. In this sense, our main result that the measured disk size is bigger than expected is robust.

5.3. The Lamp-post Model

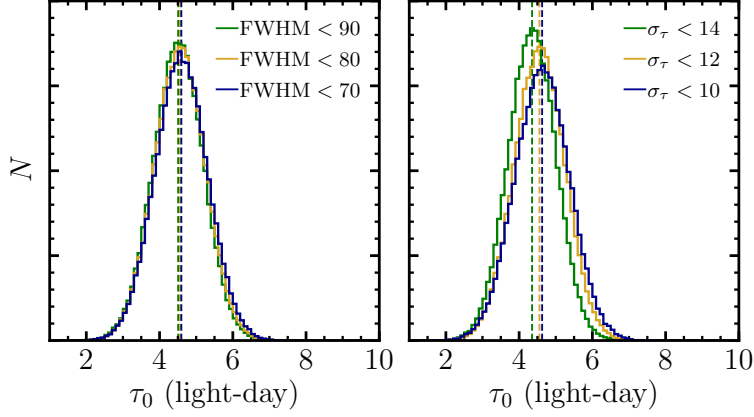


Figure 11. The distributions of the inferred disk size τ_0 under case I for different selection criteria. (Left) the ACF FWHMs of mock light curves are restricted to <90 , 80 , and 70 days. (Right) the uncertainties of time delays of mock light curves are restricted to $\sigma_\tau < 14$, 12 , and 10 days.

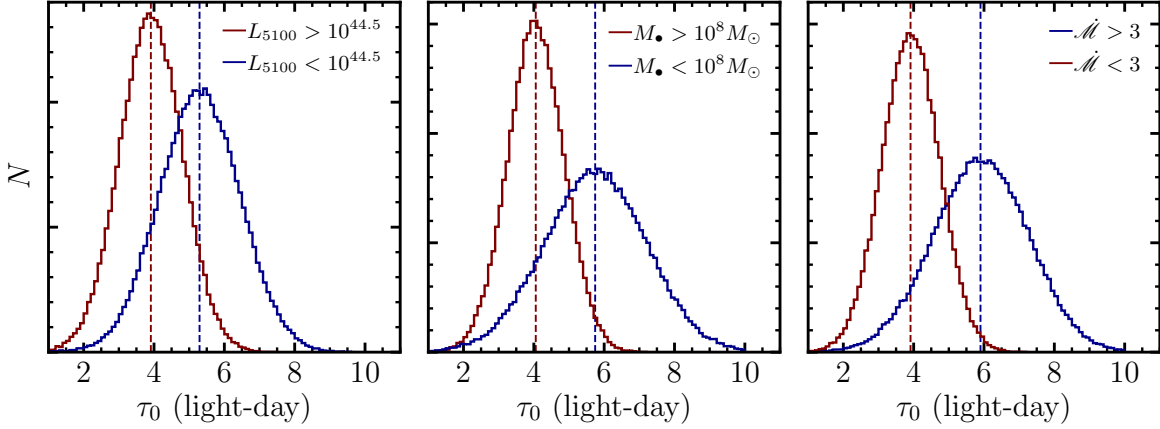


Figure 12. The posterior distributions of the disk size τ_0 under Case I for subsamples of (left) 5100 \AA luminosity $L_{5100} < 10^{44.5} \text{ erg s}^{-1}$ and $> 10^{44.5} \text{ erg s}^{-1}$, (middle) black hole mass $M_\bullet > 10^8 M_\odot$ and $< 10^8 M_\odot$, and (right) Eddington ratio $\dot{M} < 3$ and > 3 .

The lamp-post model has an additional characteristic factor κ , which describes the ratio of external to local viscous heating. The disk size in the lamp-most model is given by (e.g., Cackett et al. 2007)

$$\tau_d = \left[\frac{15GC_{bol}(3 + \kappa)}{16\eta h\pi^6 c^4} \right]^{1/3} \lambda_0^{4/3} X^{4/3} M_\bullet^{1/3} L_{5100}^{1/3}, \quad (26)$$

where $\kappa = 2(1 - A)L_X H / GM_\bullet \dot{M}$, L_X is the X-ray luminosity, H is the height of the X-ray lamp above the disk, and A is the albedo of the disk. Generally, the value of κ is on the order of unity, which means that X-ray and viscous heating contribute equal amounts of energy to the disk radiation. Therefore, we expect that compared to the standard accretion disk model, the lamp-post model does not significantly change the theoretically expected disk size.

5.4. Dependence on AGN Properties

We divide the sample into subsamples according to the 5100 \AA luminosity L_{5100} , black hole mass M_\odot , and accretion rate \dot{M} , respectively. We then repeat the above fitting

analysis of Case I for each subsample and show the posterior distributions of τ_0 in Figure 12. In the left panel, there are 46 AGNs with $L_{5100} < 10^{44.5} \text{ erg s}^{-1}$ and 46 AGNs with $L_{5100} > 10^{44.5} \text{ erg s}^{-1}$. The corresponding best estimated disk sizes are $\tau_0 = 3.91_{-0.88}^{+0.88}$ days and $5.29_{-1.14}^{+1.14}$ days, respectively. In the middle panel, we obtain the disk size $\tau_0 = 5.74_{-1.45}^{+1.45}$ days and $4.05_{-0.80}^{+0.81}$ days for the black hole mass $M_\bullet < 10^8 M_\odot$ (45 AGNs) and $> 10^8 M_\odot$ (47 AGNs). The right panel of Figure 12 compares the disk sizes for sub-Eddington ($\dot{M} < 3$) and super-Eddington ($\dot{M} > 3$) subsamples, which consist of 56 and 36 AGNs, respectively. The best estimates are $\tau_0 = 3.91_{-0.82}^{+0.82}$ days for sub-Eddington subsample and $5.90_{-1.35}^{+1.35}$ days for super-Eddington subsample. The overall large uncertainties mean that the differences between the subsamples are not significant and thereby further tests with future ZTF data releases are warranted to draw solid conclusions. However, it is worth mentioning that the recent study of Li et al. (2021) showed that low-luminosity AGNs favor large disk sizes by surveying available disk size measurements from the literature (see Figure 1 therein). This

is remarkably consistent with our results in the left panel of Figure 12.

From the theoretical point of view, we normalize the disk size to a fixed black hole mass and luminosity (thus to a fixed accretion rate; see Equations 14 and 17), therefore, we expect that the disk size τ_0 is independent on AGN properties. However, there are two possibilities that may cause the observed dependence in Figure 12. First, we adopt a constant virial factor f_{BLR} when estimating the black hole mass using Equation (1). Dynamical modeling of broad-line regions generally showed that f_{BLR} might depend on AGN properties and change from object to object (e.g., Pancoast et al. 2011, 2014; Li et al. 2013, 2018; Grier et al. 2017; Williams et al. 2018). Observational calibrations of the virial factor also tend to support this conclusion (e.g., Ho & Kim 2014; Mejía-Restrepo et al. 2018; Yu et al. 2019). If there are systematic correlations between f_{BLR} and luminosity L_{5100} , black hole mass M_\bullet , or accretion rate \dot{M} , using a constant f_{BLR} will lead to the apparent dependence of τ_0 on AGN properties. Such a bias can be eliminated once we have a solid understanding of the virial factor in the future. Second, it is possible that the disk's temperature profile does change with the accretion rate. For example, the standard and slim disk models predict different temperature profiles⁷ (Shakura & Sunyaev 1973; Abramowicz et al. 1988). There are also other physical processes that may contribute to the correlation between β and \dot{M} (e.g., see Li et al. 2021 and Kamoun et al. 2021). Figure 7 implies that τ_0 and β are highly anti-correlated. As a result, a shallower temperature profile (larger β) will lead to a smaller disk size τ_0 and vice versa. In our sample, we find that high-luminosity and high-mass black holes generally have low accretion rates, giving rise to the dependence of τ_0 on luminosity and black hole mass.

5.5. The Virial Factor

The value of the virial factor affects black hole mass estimation and thereby the expected disk size (based on the standard disk model) as

$$\tau_d \propto M_\bullet^{1/3} \propto f_{\text{BLR}}^{1/3}. \quad (27)$$

In our calculations, we adopt $f_{\text{BLR}} = 1.12 \pm 0.31$ from Woo et al. (2015). With this value, we find that the measured disk size is 1.36 and 2.06 times the theoretical expectation using a responsivity-weighted and emissivity-weighted factor, respectively. If we manually align the measured disk size with the theoretical expectation, the virial factor has to be increased to $f_{\text{BLR}} = 2.82$ and 9.80, respectively. For a disk-like BLR with an opening angle θ and inclination of i , the virial factor (in terms of FWHM) can be expressed as (e.g., Collin et al. 2006)

$$f_{\text{BLR}} \approx 0.25(\sin^2 \theta + \sin^2 i)^{-1}, \quad (28)$$

⁷ However, we note that the temperature profiles of slim disks ($T \propto R^{-1/2}$) become different from those of standard disks ($T \propto R^{-3/4}$) only within the photon-trapping radius (e.g., Wang & Zhou 1999).

where the coefficient 0.25 is owing to using FWHM as the measure of line widths. To produce a virial factor of $f_{\text{BLR}} = 2.82$ and 9.80, it is easy to gather that both the inclination and opening angles are needed to be small (say, $\lesssim 15^\circ$). This seems unreasonable in consideration of the expected diverse distribution of inclination. Also, previous BLR reverberation mapping showed evidence for a thick BLR disk, namely, a large opening angle (e.g., Peterson 2014).

5.6. The Internal Extinction of AGNs

It is clear that the AGN extinction leads to underestimation of the AGN luminosities and thereby the theoretical accretion disk size. We use the $\text{H}\alpha/\text{H}\beta$ ratio to estimate the AGN internal extinction. We limited the redshift to $z < 0.35$ so as to have both $\text{H}\alpha$ and $\text{H}\beta$ lines in the spectral wavelength coverage. There are 49 AGNs in our sample satisfying this criterion. The obtained $\text{H}\alpha/\text{H}\beta$ ratio range from 2.6 to 5.1. The median ratio is 3.55, generally consistent with that of the SDSS DR7 AGN sample (Baron et al. 2016).

If presuming the intrinsic $\text{H}\alpha/\text{H}\beta$ ratio to be 2.72 as in Gaskell (2017), the median ratio of 3.55 corresponds to extinction of $E(B - V) = 0.21$ using the gray dust model of Gaskell (2017). This leads to the intrinsic luminosity at 5100 Å larger by a factor of 0.9-2.0 with $R_V = 3.1 - 5.5$ (Gaskell & Benker 2007). As a result, the estimated black hole mass will be larger by 10%-18% (Equation 1). The theoretical disk size will be increased to 3.05-3.80 days with the emissivity-weighted factor and 4.57-5.68 days with the responsivity-weighted factor. The latter case can explain the measured disk sizes while in the former case the theoretical disk size is still a bit smaller. As a comparison, if using the extinction curve of the Milky Way (Pei 1992), the resulting extinction is $E(B - V) = 0.16$. The intrinsic luminosity at 5100 Å will be larger by a factor of 0.6-1.2 with $R_V = 3.1 - 5.5$. With the emissivity-weighted (responsivity-weighted) factor, the theoretical disk size is changed to 2.84-3.20 (3.19-4.80) light-days.

We note that there are still debates on quantitatively estimating the AGN extinction (e.g., McKee & Petrosian 1974; Netzer & Davidson 1979; de Zotti & Gaskell 1985; Gaskell & Benker 2007; Ferland et al. 2013). It seems that the recipe of Gaskell (2017) gives a relatively large extinction, which can be regarded as an upper conservative limit.

6. CONCLUSIONS

We compile a sample of 92 AGNs with *gri* photometric light curves from the ZTF DR3 archival data and measure their inter-band time delays with the ICCF method. We also use the MICA method (Li et al. 2016) and von Neumann estimator (Chelouche et al. 2017) to cross check the ICCF delays and find the general consistency (see Appendix C). We then employ a generalized accretion disk model to fit these time delays with a Markov-chain Monte Carlo technique and put constraints on the disk temperature profile, characteristic disk size, and its dependence on black hole mass and accretion rate. The present sample does not allow us to simultaneously determine the full parameters (the disk size parameter

τ_0 , the temperature profile parameter β , and the parameters γ and δ for the dependence on black hole mass and luminosity; see Equation 15). We design three cases by fixing some parameters according to the energy equation of the generalized disk model (see Equation 16). Below by saying the disk size, we refer to the size normalized to a black hole mass of $10^8 M_\odot$ and luminosity of $10^{44.5} \text{ erg s}^{-1}$ (see Equation 15). Our main results are summarized as follows.

- The best estimated disk size is $\tau_0 = 4.56_{-0.69}^{+0.69}$ light-days. This is 1.36 times as large as the theoretical expectation 3.35 light-days of the standard accretion disk model (namely, steady-state, optically thick, geometrically thin, and with a Keplerian rotation) at a 2σ level if using the responsivity-weighted factor $\chi = 5.04$ and 2.06 times the theoretic predication 2.24 light-days at a 3σ level if using the emissivity-weighted factor $\chi = 3.36$.
- The disk temperature profile parameter $\beta = 1.08_{-0.57}^{+0.61}$, consistent within uncertainties with the value of $4/3$ for the standard accretion disk model.
- The dependence of inter-band time delays on luminosity has a power index of $\delta = 0.44_{-0.22}^{+0.19}$, agreeing with the theoretical expectation of $1/3$. However, the dependence on black hole mass has a power index of $\gamma = 0.06_{-0.15}^{+0.15}$, deviating from the expected value of $1/3$. This may be due to assuming a constant virial factor f_{BLR} and its possible dependence on black hole mass is neglected.
- Our results tentatively show that the (normalized) disk size might depend on black hole mass, luminosity, and accretion rate (see Figure 12). However, considering the large uncertainties, this warrants future tests with more high-quality data for further confirmation.

These results are broadly in agreement with previous studies based on large AGN samples (e.g., Jiang et al. 2017; Homayouni et al. 2021; Jha et al. 2021) or individual AGNs

with intensive monitoring (e.g., Fausnaugh et al. 2016; Cackett et al. 2018; Edelson et al. 2019). Nevertheless, we remark that 1) inclusion of the intrinsic AGN extinction may partially reconcile the discrepancy of accretion disk sizes, although there is no consensus on quantitatively estimating the extinction; and 2) limited by the sample size, our results bear larger uncertainties. With increasing data accumulation of the ZTF, future larger AGN samples will place more restricted constraints on the disk properties.

Software: DASpec (<https://github.com/PuDu-Astro/DASpec>), MICA (Li et al. 2016), CDNest (Li 2020), emcee (Foreman-Mackey et al. 2013)

ACKNOWLEDGEMENTS

We thank the referee for useful comments that significantly improve the manuscript. We thank P. Du and C. Hu for valuable advice. We acknowledge financial support from the National Natural Science Foundation of China (11833008 and 11991054), from the National Key Research and Development Program of China (2016YFA0400701), and from China Manned Space Project (CMS-CSST-2021-A06 and CMS-CSST-2021-B11). Y.-R.L. acknowledges financial support from the National Natural Science Foundation of China through Grant No. 11922304, from the Strategic Priority Research Program of CAS through Grant No. XDB23000000, and from the Youth Innovation Promotion Association CAS. L.C.H. acknowledges financial support from the National Science Foundation of China (11721303 and 11991052) and the National Key Research and Development Program of China (2016YFA0400702).

The Zwicky Transient Facility Collaboration is supported by U.S. National Science Foundation through the Mid-Scale Innovations Program (MSIP). This research has made use of the NASA/IPAC Extragalactic Database (NED) which is operated by the Jet Propulsion Laboratory, California Institute of Technology, under contract with the National Aeronautics and Space.

APPENDIX

A. SIMULATION TESTS ON THE INFLUENCES OF BROAD EMISSION LINES AND DATA SAMPLING

In Section 2.4, we perform Monte Carlo simulations to test the influences of broad emission lines and data sampling on the observed time delays and select those AGNs with minimized influences. Here, for the sake of illustration, we show an example of mock light curves and ICCF analysis in Figure 13. The mock light curves are generated according to the observed data in Figure 1.

In addition, we perform simulations to quantitatively illustrate how broad emission lines affect the time delay measurements. Without loss of generality, we adopt a characteristic time delay of 2 days for between two bands (say, e.g., g and r bands or g and i bands) and 65 days for broad emission lines according to the median black hole mass and 5100 \AA luminosity of our sample. Given a pair of flux fractions of broad emission lines in two bands, we use the same procedure described in Section 2.4 to generate 1000 sets of light curves. The sampling rate is overall set to 3 days apart. We then use the ICCF method to calculate time delays and derive the mean time delay for the simulated light curves. In Figure 14, we plot the differences between output (τ_{out}) and input (τ_{in}) time delays for different flux fractions of broad emissions lines. We also superimpose the observed fractions of broad emission lines in g , r , and i bands for our sample. As can be seen, the majority of AGNs in our sample are located within the

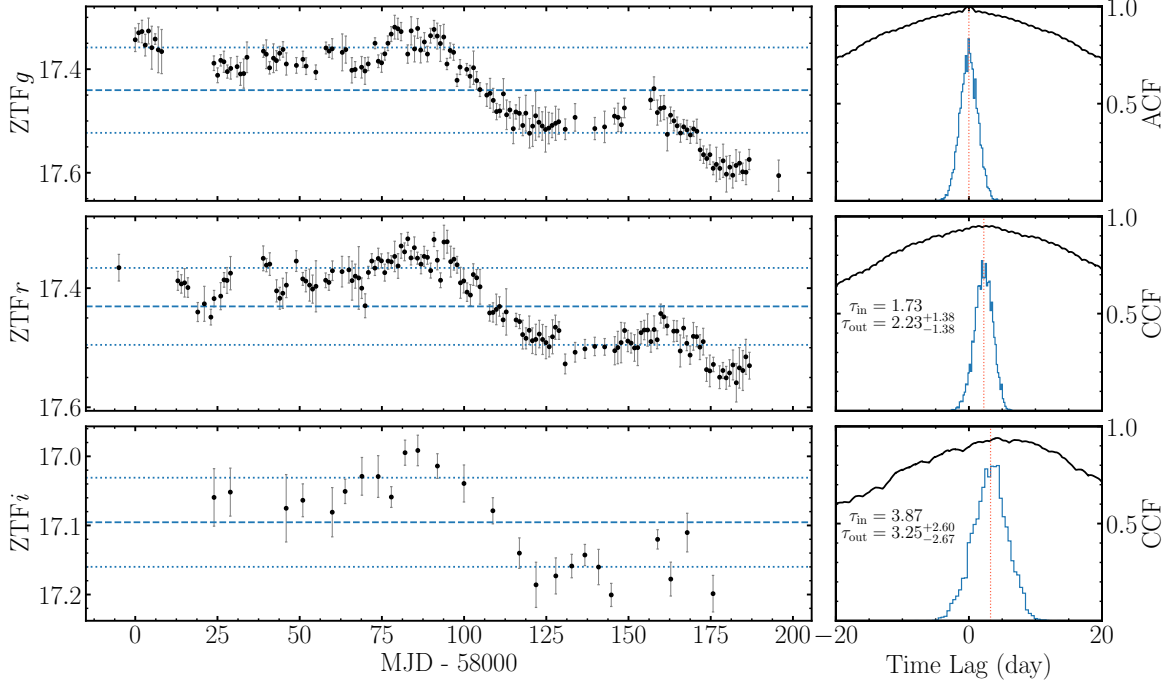


Figure 13. (Left) an example of mock g -, r - and i -band light curves generated according to the observed data in Figure 1. (Right) from top to bottom panels are the ACF of the g -band mock light curve and the ICCFs of r - and i -band mock light curves with respect to g -band one, respectively. The histograms represent the cross-correlation centroid distributions. The input and output time delays (in units of days) for r - and i -band are also marked in each panel.

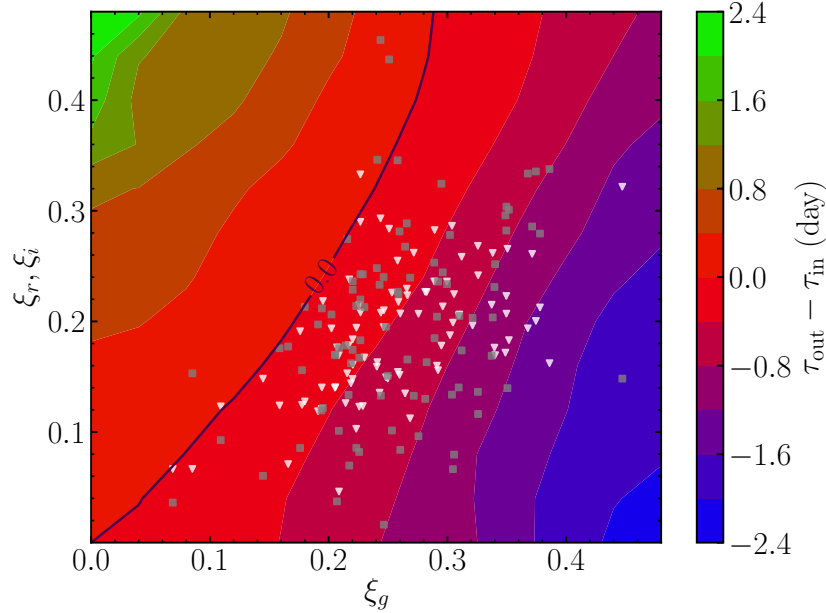


Figure 14. Differences between output and input time delays of two (arbitrary) bands using simulated light curves for different flux fraction of broad emission lines (see Appendix A for a detail). Superimposed are the observed flux fractions of broad emission lines in g , r , and i bands for our AGN sample. White squares and gray triangles represent r and i bands, respectively.

region of $\tau_{out} - \tau_{in} < 0$, indicating that the presence of broad emission lines tends to shorten the measured time delays than the realistic values.

B. CALCULATING THE MULTIPLICATIVE FACTORS

In this section, we show how to calculate the multiplicative factors defined in Section 3.3. We first introduce a new variable $x = hc/kT\lambda$. With a temperature profile $T \propto R^{-1/\beta}$, we have

$$R \propto x^\beta \text{ and } dR \propto x^{\beta-1} dx. \quad (\text{B1})$$

As a result, the emissivity-weighted factor can be recasted as

$$\chi_e = \frac{1}{R_\lambda} \frac{\int_{R_{\text{in}}}^{R_{\text{out}}} B_\lambda(T) R^2 dR}{\int_{R_{\text{in}}}^{R_{\text{out}}} B_\lambda(T) R dR} = \frac{\int_{x_{\text{in}}}^{x_{\text{out}}} \frac{1}{e^x - 1} x^{3\beta-1} dx}{\int_{x_{\text{in}}}^{x_{\text{out}}} \frac{1}{e^x - 1} x^{2\beta-1} dx}, \quad (\text{B2})$$

where x_{in} and x_{out} represent the values of x at inner and outer disk radius. In the case of $x_{\text{in}} = 0$ and $x_{\text{out}} = \infty$, with the integral formula (Abramowitz & Stegun 1972)

$$\int_0^\infty \frac{x^n}{e^x - 1} dx = \zeta(n+1)\Gamma(n+1), \quad (\text{B3})$$

the emissivity-weighted factor can be analytically expressed as

$$\chi_e = \frac{\zeta(3\beta)\Gamma(3\beta)}{\zeta(2\beta)\Gamma(2\beta)}, \quad (\text{B4})$$

where $\zeta(x)$ and $\Gamma(x)$ are the zeta function and gamma function respectively (Abramowitz & Stegun 1972). As can be seen, the black hole mass and accretion rate do not appear in the far right-hand side of Equation (B2). Therefore, χ_e is independent on black hole mass and accretion rate.

Similarly, we can recast the expression for the responsivity-weighted factor χ_r as

$$\chi_r = \frac{1}{R_\lambda} \frac{\int_{R_{\text{in}}}^{R_{\text{out}}} \frac{\partial B_\lambda(T)}{\partial T} \frac{\partial T}{\partial f_c} R^2 dR}{\int_{R_{\text{in}}}^{R_{\text{out}}} \frac{\partial B_\lambda(T)}{\partial T} \frac{\partial T}{\partial f_c} R dR} = \frac{\int_{x_{\text{in}}}^{x_{\text{out}}} \frac{e^x}{(e^x - 1)^2} x^{3\beta} dx}{\int_{x_{\text{in}}}^{x_{\text{out}}} \frac{e^x}{(e^x - 1)^2} x^{2\beta} dx}. \quad (\text{B5})$$

Again, with the aid of the zeta and gamma functions, we have

$$\chi_r = \frac{\zeta(3\beta)\Gamma(3\beta+1)}{\zeta(2\beta)\Gamma(2\beta+1)}, \quad (\text{B6})$$

where we used the integral formula

$$\int_0^\infty \frac{e^x x^n}{(e^x - 1)^2} dx = \zeta(n)\Gamma(n+1). \quad (\text{B7})$$

C. TIME DELAY MEASUREMENTS FROM THE MICA AND VON NEUMANN ESTIMATOR

Figure 15 compares the measured inter-band time delays from the ICCF method with those from the MICA method and the von Neumann estimator. We can find general consistency among the three approaches. The uncertainties of τ_{gr} obtained by MICA are a factor of 0.74 of those obtained by the ICCF method, whereas the uncertainties of τ_{gi} obtained by the two methods are comparable. The uncertainties from the von Neumann estimator are overall 1.32 times larger than those from the ICCF method.

We also run the fitting analysis using time delays from MICA and von Neumann estimator. Table 5 compares the obtained results from ICCF, MICA, and von Neumann estimator, which, again, are consistent within uncertainties among the three approaches. In Figure 16, we plot the fitting results of Case III using the MICA-based time delays. As expected, the best estimates of parameter τ_0 , δ , and γ are consistent with the ICCF results but have relatively smaller uncertainties.

REFERENCES

- Abramowicz, M. A., Czerny, B., Lasota, J. P., & Szuszkiewicz, E. 1988, *ApJ*, 332, 646, doi: [10.1086/166683](https://doi.org/10.1086/166683)
- Abramowitz, M., & Stegun, I. A. 1972, *Handbook of Mathematical Functions* (New York: Dover), 255–807

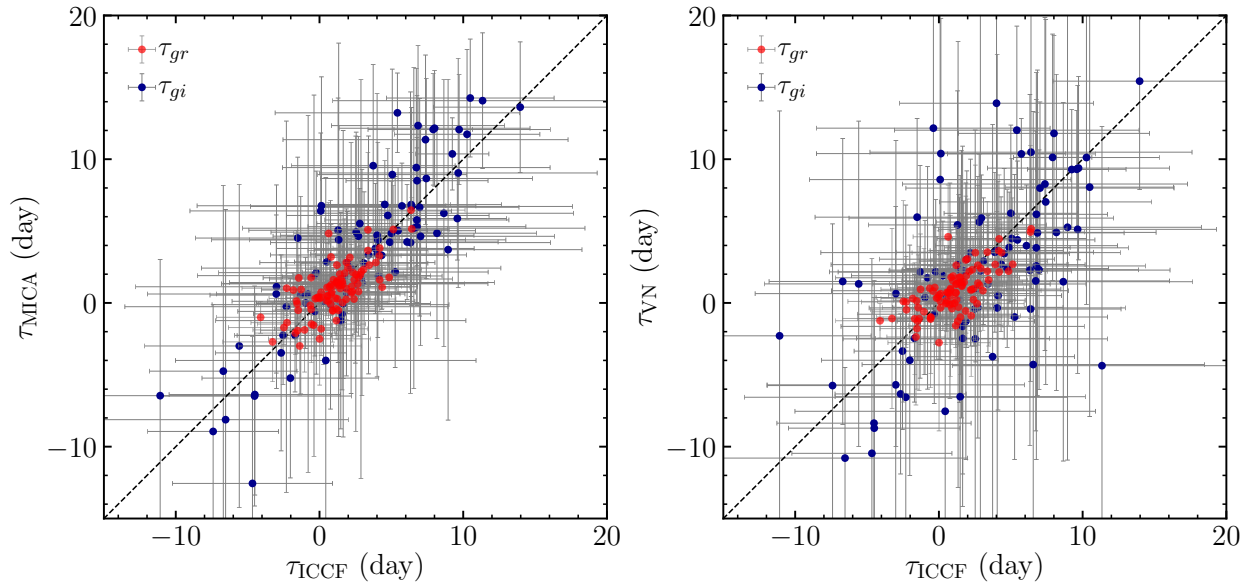


Figure 15. Comparisons of inter-band time delays measured by the ICCF method with (left) the MICA method and (right) von Neumann Esitimator. The orange and blue points represent τ_{gr} and τ_{gi} (in the observed frame), respectively.

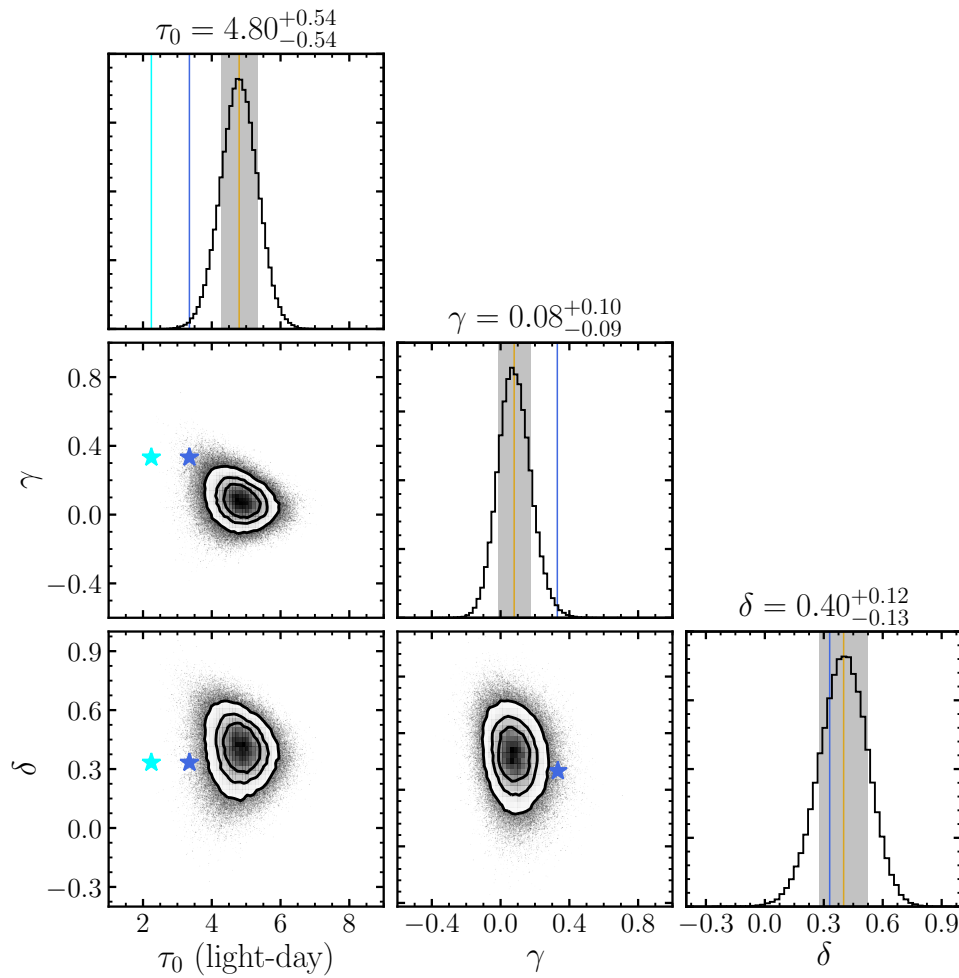


Figure 16. Same as Figure 8, but using the MICA-based inter-band time delays.

Table 5. The best estimated disk parameters using ICCF, MICA, and von Neumann estimator.

	Parameter	ICCF	MICA	von Neumann Estimator	Theoretical Value
Case I	τ_0 (light-day)	$4.56^{+0.69}_{-0.69}$	$4.23^{+0.43}_{-0.43}$	$4.31^{+0.79}_{-0.79}$	2.24 (3.36)
Case II	τ_0 (light-day)	$5.29^{+4.05}_{-1.69}$	$5.12^{+2.05}_{-1.15}$	$5.72^{+5.97}_{-2.26}$	2.24 (3.36)
	β	$1.08^{+0.61}_{-0.57}$	$1.02^{+0.38}_{-0.36}$	$0.93^{+0.69}_{-0.54}$	4/3
Case III	τ_0 (light-day)	$4.68^{+0.88}_{-0.91}$	$4.80^{+0.54}_{-0.54}$	$4.55^{+1.00}_{-1.04}$	2.24 (3.36)
	γ	$0.06^{+0.15}_{-0.15}$	$0.08^{+0.10}_{-0.09}$	$0.05^{+0.20}_{-0.17}$	1/3
	δ	$0.44^{+0.19}_{-0.22}$	$0.40^{+0.12}_{-0.13}$	$0.35^{+0.24}_{-0.25}$	1/3

NOTE—Two theoretical values of τ_0 represent the disk sizes using emissivity- and responsivity-weighted factor, respectively.

- Baron, D., Stern, J., Poznanski, D., & Netzer, H. 2016, *ApJ*, 832, 8, doi: [10.3847/0004-637X/832/1/8](https://doi.org/10.3847/0004-637X/832/1/8)
- Barth, A. J., Pancoast, A., Bennert, V. N., et al. 2013, *ApJ*, 769, 128, doi: [10.1088/0004-637X/769/2/128](https://doi.org/10.1088/0004-637X/769/2/128)
- Bellm, E. C., Kulkarni, S. R., Graham, M. J., et al. 2019, *PASP*, 131, 018002, doi: [10.1088/1538-3873/aacbe](https://doi.org/10.1088/1538-3873/aacbe)
- Bentz, M. C., Peterson, B. M., Netzer, H., Pogge, R. W., & Vestergaard, M. 2009, *ApJ*, 697, 160, doi: [10.1088/0004-637X/697/1/160](https://doi.org/10.1088/0004-637X/697/1/160)
- Bentz, M. C., Denney, K. D., Grier, C. J., et al. 2013, *ApJ*, 767, 149, doi: [10.1088/0004-637X/767/2/149](https://doi.org/10.1088/0004-637X/767/2/149)
- Blaes, O. 2007, in *Astronomical Society of the Pacific Conference Series*, Vol. 373, *The Central Engine of Active Galactic Nuclei*, ed. L. C. Ho & J. W. Wang, 75. <https://arxiv.org/abs/astro-ph/0703589>
- Boroson, T. A., & Green, R. F. 1992, *ApJS*, 80, 109, doi: [10.1086/191661](https://doi.org/10.1086/191661)
- Brewer, B. J., Pártay, L. B., & Csányi, G. 2011, *Statistics and Computing* volume, arXiv:2109.05036, doi: [10.1007/s11222-010-9198-8](https://doi.org/10.1007/s11222-010-9198-8)
- Bruzual, G., & Charlot, S. 2003, *MNRAS*, 344, 1000, doi: [10.1046/j.1365-8711.2003.06897.x](https://doi.org/10.1046/j.1365-8711.2003.06897.x)
- Cackett, E. M., Chiang, C.-Y., McHardy, I., et al. 2018, *ApJ*, 857, 53, doi: [10.3847/1538-4357/aab4f7](https://doi.org/10.3847/1538-4357/aab4f7)
- Cackett, E. M., Horne, K., & Winkler, H. 2007, *MNRAS*, 380, 669, doi: [10.1111/j.1365-2966.2007.12098.x](https://doi.org/10.1111/j.1365-2966.2007.12098.x)
- Cackett, E. M., Gelbord, J., Li, Y.-R., et al. 2020, *ApJ*, 896, 1, doi: [10.3847/1538-4357/ab91b5](https://doi.org/10.3847/1538-4357/ab91b5)
- Chelouche, D., Pozo-Nuñez, F., & Zucker, S. 2017, *ApJ*, 844, 146, doi: [10.3847/1538-4357/aa7b86](https://doi.org/10.3847/1538-4357/aa7b86)
- Collier, S., Horne, K., Wanders, I., & Peterson, B. M. 1999, *MNRAS*, 302, L24, doi: [10.1046/j.1365-8711.1999.02250.x](https://doi.org/10.1046/j.1365-8711.1999.02250.x)
- Collin, S., Kawaguchi, T., Peterson, B. M., & Vestergaard, M. 2006, *A&A*, 456, 75, doi: [10.1051/0004-6361:20064878](https://doi.org/10.1051/0004-6361:20064878)
- Cornachione, M. A., & Morgan, C. W. 2020, *ApJ*, 895, 93, doi: [10.3847/1538-4357/ab8aed](https://doi.org/10.3847/1538-4357/ab8aed)
- Courvoisier, T. J. L., & Clavel, J. 1991, *A&A*, 248, 389
- de Zotti, G., & Gaskell, C. M. 1985, *A&A*, 147, 1
- Du, P., & Wang, J.-M. 2019, *ApJ*, 886, 42, doi: [10.3847/1538-4357/ab4908](https://doi.org/10.3847/1538-4357/ab4908)
- Du, P., Wang, J.-M., Hu, C., et al. 2016, *ApJL*, 818, L14, doi: [10.3847/2041-8205/818/1/L14](https://doi.org/10.3847/2041-8205/818/1/L14)
- Du, P., Hu, C., Lu, K.-X., et al. 2014, *ApJ*, 782, 45, doi: [10.1088/0004-637X/782/1/45](https://doi.org/10.1088/0004-637X/782/1/45)
- Edelson, R., Gelbord, J., Cackett, E., et al. 2019, *ApJ*, 870, 123, doi: [10.3847/1538-4357/aaf3b4](https://doi.org/10.3847/1538-4357/aaf3b4)
- Fausnaugh, M. M., Denney, K. D., Barth, A. J., et al. 2016, *ApJ*, 821, 56, doi: [10.3847/0004-637X/821/1/56](https://doi.org/10.3847/0004-637X/821/1/56)
- Fausnaugh, M. M., Starkey, D. A., Horne, K., et al. 2018, *ApJ*, 854, 107, doi: [10.3847/1538-4357/aaa2b](https://doi.org/10.3847/1538-4357/aaa2b)
- Ferland, G. J., Porter, R. L., van Hoof, P. A. M., et al. 2013, *RMxAA*, 49, 137. <https://arxiv.org/abs/1302.4485>
- Fischer, T. C., Crenshaw, D. M., Kraemer, S. B., Schmitt, H. R., & Turner, T. J. 2014, *ApJ*, 785, 25, doi: [10.1088/0004-637X/785/1/25](https://doi.org/10.1088/0004-637X/785/1/25)
- Foreman-Mackey, D., Hogg, D. W., Lang, D., & Goodman, J. 2013, *PASP*, 125, 306, doi: [10.1086/670067](https://doi.org/10.1086/670067)
- Gaskell, C. M. 2017, *MNRAS*, 467, 226, doi: [10.1093/mnras/stx094](https://doi.org/10.1093/mnras/stx094)
- Gaskell, C. M., & Benker, A. J. 2007, arXiv e-prints, arXiv:0711.1013. <https://arxiv.org/abs/0711.1013>
- Gaskell, C. M., & Peterson, B. M. 1987, *ApJS*, 65, 1, doi: [10.1086/191216](https://doi.org/10.1086/191216)
- Gaskell, C. M., & Sparke, L. S. 1986, *ApJ*, 305, 175, doi: [10.1086/164238](https://doi.org/10.1086/164238)
- Gierliński, M., & Done, C. 2004, *MNRAS*, 347, 885, doi: [10.1111/j.1365-2966.2004.07266.x](https://doi.org/10.1111/j.1365-2966.2004.07266.x)
- Graham, M. J., Kulkarni, S. R., Bellm, E. C., et al. 2019, *PASP*, 131, 078001, doi: [10.1088/1538-3873/ab006c](https://doi.org/10.1088/1538-3873/ab006c)
- Grier, C. J., Pancoast, A., Barth, A. J., et al. 2017, *ApJ*, 849, 146, doi: [10.3847/1538-4357/aa901b](https://doi.org/10.3847/1538-4357/aa901b)
- Hernández Santisteban, J. V., Edelson, R., Horne, K., et al. 2020, *MNRAS*, 498, 5399, doi: [10.1093/mnras/staa2365](https://doi.org/10.1093/mnras/staa2365)

- Ho, L. C., & Kim, M. 2014, *ApJ*, 789, 17, doi: [10.1088/0004-637X/789/1/17](https://doi.org/10.1088/0004-637X/789/1/17)
- Homayouni, Y., Trump, J. R., Grier, C. J., et al. 2019, *ApJ*, 880, 126, doi: [10.3847/1538-4357/ab2638](https://doi.org/10.3847/1538-4357/ab2638)
- Homayouni, Y., Sturm, M. R., Trump, J. R., et al. 2021, arXiv e-prints, arXiv:2105.02884. <https://arxiv.org/abs/2105.02884>
- Hu, C., Du, P., Lu, K.-X., et al. 2015, *ApJ*, 804, 138, doi: [10.1088/0004-637X/804/2/138](https://doi.org/10.1088/0004-637X/804/2/138)
- Jha, V. K., Joshi, R., Chand, H., et al. 2021, arXiv e-prints, arXiv:2109.05036. <https://arxiv.org/abs/2109.05036>
- Jiang, Y.-F., Green, P. J., Greene, J. E., et al. 2017, *ApJ*, 836, 186, doi: [10.3847/1538-4357/aa5b91](https://doi.org/10.3847/1538-4357/aa5b91)
- Kammoun, E. S., Dovčiak, M., Papadakis, I. E., Caballero-García, M. D., & Karas, V. 2021, *ApJ*, 907, 20, doi: [10.3847/1538-4357/abcb93](https://doi.org/10.3847/1538-4357/abcb93)
- Kara, E., Mehdipour, M., Kriss, G. A., et al. 2021, arXiv e-prints, arXiv:2105.05840. <https://arxiv.org/abs/2105.05840>
- Kasliwal, V. P., Vogeley, M. S., & Richards, G. T. 2015, *MNRAS*, 451, 4328, doi: [10.1093/mnras/stv1230](https://doi.org/10.1093/mnras/stv1230)
- Kelly, B. C., Bechtold, J., & Siemiginowska, A. 2009, *ApJ*, 698, 895, doi: [10.1088/0004-637X/698/1/895](https://doi.org/10.1088/0004-637X/698/1/895)
- Kishimoto, M., Antonucci, R., Blaes, O., et al. 2008, *Nature*, 454, 492, doi: [10.1038/nature07114](https://doi.org/10.1038/nature07114)
- Kochanek, C. S. 2004, *ApJ*, 605, 58, doi: [10.1086/382180](https://doi.org/10.1086/382180)
- Koratkar, A., & Blaes, O. 1999, *PASP*, 111, 1, doi: [10.1086/316294](https://doi.org/10.1086/316294)
- Li, T., Sun, M., Xu, X., et al. 2021, *ApJL*, 912, L29, doi: [10.3847/2041-8213/abf9aa](https://doi.org/10.3847/2041-8213/abf9aa)
- Li, Y.-R. 2020, *LiyraAstroph/CDNest*: CDNest: A diffusive nested sampling code in C, v0.2.0, Zenodo, doi: [10.5281/zenodo.3884449](https://doi.org/10.5281/zenodo.3884449)
- Li, Y.-R., Wang, J.-M., & Bai, J.-M. 2016, *ApJ*, 831, 206, doi: [10.3847/0004-637X/831/2/206](https://doi.org/10.3847/0004-637X/831/2/206)
- Li, Y.-R., Wang, J.-M., Ho, L. C., Du, P., & Bai, J.-M. 2013, *ApJ*, 779, 110, doi: [10.1088/0004-637X/779/2/110](https://doi.org/10.1088/0004-637X/779/2/110)
- Li, Y.-R., Songsheng, Y.-Y., Qiu, J., et al. 2018, *ApJ*, 869, 137, doi: [10.3847/1538-4357/aaee6b](https://doi.org/10.3847/1538-4357/aaee6b)
- Lin, D. N. C., & Papaloizou, J. C. B. 1996, *ARA&A*, 34, 703, doi: [10.1146/annurev.astro.34.1.703](https://doi.org/10.1146/annurev.astro.34.1.703)
- Lobban, A. P., Zola, S., Pajdosz-Śmierciak, U., et al. 2020, *MNRAS*, 494, 1165, doi: [10.1093/mnras/staa630](https://doi.org/10.1093/mnras/staa630)
- Masci, F. J., Laher, R. R., Rusholme, B., et al. 2019, *PASP*, 131, 018003, doi: [10.1088/1538-3873/aae8ac](https://doi.org/10.1088/1538-3873/aae8ac)
- McHardy, I. M., Connolly, S. D., Horne, K., et al. 2018, *MNRAS*, 480, 2881, doi: [10.1093/mnras/sty1983](https://doi.org/10.1093/mnras/sty1983)
- McKee, C. F., & Petrosian, V. 1974, *ApJ*, 189, 17, doi: [10.1086/152763](https://doi.org/10.1086/152763)
- Mejía-Restrepo, J. E., Lira, P., Netzer, H., Trakhtenbrot, B., & Capellupo, D. M. 2018, *Nature Astronomy*, 2, 63, doi: [10.1038/s41550-017-0305-z](https://doi.org/10.1038/s41550-017-0305-z)
- Morgan, C. W., Kochanek, C. S., Morgan, N. D., & Falco, E. E. 2006, *ApJ*, 647, 874, doi: [10.1086/505569](https://doi.org/10.1086/505569)
- Morgan, C. W., Kochanek, C. S., Morgan, N. D., & Falco, E. E. 2010, *ApJ*, 712, 1129, doi: [10.1088/0004-637X/712/2/1129](https://doi.org/10.1088/0004-637X/712/2/1129)
- Mudd, D., Martini, P., Zu, Y., et al. 2018, *ApJ*, 862, 123, doi: [10.3847/1538-4357/aac9bb](https://doi.org/10.3847/1538-4357/aac9bb)
- Netzer, H., & Davidson, K. 1979, *MNRAS*, 187, 871, doi: [10.1093/mnras/187.4.871](https://doi.org/10.1093/mnras/187.4.871)
- Pancoast, A., Brewer, B. J., & Treu, T. 2011, *ApJ*, 730, 139, doi: [10.1088/0004-637X/730/2/139](https://doi.org/10.1088/0004-637X/730/2/139)
- . 2014, *MNRAS*, 445, 3055, doi: [10.1093/mnras/stu1809](https://doi.org/10.1093/mnras/stu1809)
- Pâris, I., Petitjean, P., Aubourg, É., et al. 2018, *A&A*, 613, A51, doi: [10.1051/0004-6361/201732445](https://doi.org/10.1051/0004-6361/201732445)
- Pei, Y. C. 1992, *ApJ*, 395, 130, doi: [10.1086/171637](https://doi.org/10.1086/171637)
- Peterson, B. M. 1993, *PASP*, 105, 247, doi: [10.1086/133140](https://doi.org/10.1086/133140)
- . 2014, *SSRv*, 183, 253, doi: [10.1007/s11214-013-9987-4](https://doi.org/10.1007/s11214-013-9987-4)
- Peterson, B. M., Wanders, I., Horne, K., et al. 1998, *PASP*, 110, 660, doi: [10.1086/316177](https://doi.org/10.1086/316177)
- Peterson, B. M., Ferrarese, L., Gilbert, K. M., et al. 2004, *ApJ*, 613, 682, doi: [10.1086/423269](https://doi.org/10.1086/423269)
- Planck Collaboration, Aghanim, N., Akrami, Y., et al. 2020, *A&A*, 641, A6, doi: [10.1051/0004-6361/201833910](https://doi.org/10.1051/0004-6361/201833910)
- Sánchez-Sáez, P., Lira, P., Mejía-Restrepo, J., et al. 2018, *ApJ*, 864, 87, doi: [10.3847/1538-4357/aa7f9](https://doi.org/10.3847/1538-4357/aa7f9)
- Sanders, D. B., Phinney, E. S., Neugebauer, G., Soifer, B. T., & Matthews, K. 1989, *ApJ*, 347, 29, doi: [10.1086/168094](https://doi.org/10.1086/168094)
- Shakura, N. I., & Sunyaev, R. A. 1973, *A&A*, 500, 33
- Shen, Y., Greene, J. E., Strauss, M. A., Richards, G. T., & Schneider, D. P. 2008, *ApJ*, 680, 169, doi: [10.1086/587475](https://doi.org/10.1086/587475)
- Starkey, D., Horne, K., Fausnaugh, M. M., et al. 2017, *ApJ*, 835, 65, doi: [10.3847/1538-4357/835/1/65](https://doi.org/10.3847/1538-4357/835/1/65)
- Starkey, D. A., Horne, K., & Villforth, C. 2016, *MNRAS*, 456, 1960, doi: [10.1093/mnras/stv2744](https://doi.org/10.1093/mnras/stv2744)
- Tie, S. S., & Kochanek, C. S. 2018, *MNRAS*, 473, 80, doi: [10.1093/mnras/stx2348](https://doi.org/10.1093/mnras/stx2348)
- Wang, J.-M., Szuszkiewicz, E., Lu, F.-J., & Zhou, Y.-Y. 1999, *ApJ*, 522, 839, doi: [10.1086/307686](https://doi.org/10.1086/307686)
- Wang, J.-M., & Zhou, Y.-Y. 1999, *ApJ*, 516, 420, doi: [10.1086/307080](https://doi.org/10.1086/307080)
- Williams, P. R., Pancoast, A., Treu, T., et al. 2018, *ApJ*, 866, 75, doi: [10.3847/1538-4357/aae086](https://doi.org/10.3847/1538-4357/aae086)
- Woo, J.-H., Yoon, Y., Park, S., Park, D., & Kim, S. C. 2015, *ApJ*, 801, 38, doi: [10.1088/0004-637X/801/1/38](https://doi.org/10.1088/0004-637X/801/1/38)
- Yu, L.-M., Bian, W.-H., Wang, C., Zhao, B.-X., & Ge, X. 2019, *MNRAS*, 488, 1519, doi: [10.1093/mnras/stz1766](https://doi.org/10.1093/mnras/stz1766)
- Yu, Z., Martini, P., Davis, T. M., et al. 2020, *ApJS*, 246, 16, doi: [10.3847/1538-4365/ab5e7a](https://doi.org/10.3847/1538-4365/ab5e7a)
- Zu, Y., Kochanek, C. S., Kozłowski, S., & Udalski, A. 2013, *ApJ*, 765, 106, doi: [10.1088/0004-637X/765/2/106](https://doi.org/10.1088/0004-637X/765/2/106)